December 2023

Investigation of the Chemical and Electronic Structure of a 2H Phase MoS_2 Single Crystal

Mary Blankenship
University of Nevada, Las Vegas

Repository Citation

Blankenship, Mary, "Investigation of the Chemical and Electronic Structure of a 2H Phase MoS_2 Single Crystal" (2023). *UNLV Theses, Dissertations, Professional Papers, and Capstones*. 4868.
http://dx.doi.org/10.34917/37200494

INVESTIGATION OF THE CHEMICAL AND ELECTRONIC STRUCTURE OF A 2H PHASE MOS$_2$ SINGLE CRYSTAL

By

Mary Blankenship

Bachelor of Science – Chemistry
Bachelor of Arts – Economics
University of Nevada, Las Vegas
2021

A thesis submitted in partial fulfillment
of the requirements for the

Master of Science – Chemistry

Department of Chemistry and Biochemistry
College of Sciences
The Graduate College

University of Nevada, Las Vegas
December 2023

UNLV | GRADUATE COLLEGE

Thesis Approval

The Graduate College
The University of Nevada, Las Vegas

November 27, 2023

This thesis prepared by

Mary Blankenship

entitled

Investigation of the Chemical and Electronic Structure of a 2H Phase MoS_2 Single Crystal

is approved in partial fulfillment of the requirements for the degree of

Master of Science – Chemistry
Department of Chemistry and Biochemistry

Clemens Heske, Ph.D.
Examination Committee Chair

Balakrishnan Naduvalath, Ph.D.
Examination Committee Member

Dong-Chan Lee, Ph.D.
Examination Committee Member

Joshua Island, Ph.D.
Graduate College Faculty Representative

Alyssa Crittenden, Ph.D.
Vice Provost for Graduate Education &
Dean of the Graduate College

ABSTRACT

Investigation of the chemical and electronic structure of a 2H phase MoS_2 single crystal

By
Mary Blankenship

Dr. Clemens Heske, Examination Committee Chair
Professor of Chemistry
University of Nevada, Las Vegas

Molybdenum disulfide has a wide range of applications in energy conversion devices, like thin-film solar cells, batteries, bio sensors, and more. Although the properties of MoS_2 and other transition metal dichalcogenides (TMDC) have been widely studied, disagreements and discrepancies regarding its electronic structure remain.

In this thesis, a highly-oriented synthetic 2H phase MoS_2 single crystal is investigated using a toolchest of spectroscopic techniques to uncover its chemical and electronic properties. Lab-based x-ray photoelectron spectroscopy (XPS), ultraviolet photoelectron spectroscopy (UPS), inverse photoemission spectroscopy (IPES), and low energy electron diffraction (LEED) were performed at UNLV and combined with resonant inelastic soft x-ray scattering (RIXS) at the Advanced Light Source (ALS), Lawrence Berkeley National Laboratory. Together with theoretical calculations of the density of states and band structure, an in-depth picture of MoS_2 properties is painted. In addition, the effects of mechanical exfoliation on the chemical and electronic environment of the MoS_2 crystal surface is discussed. The results are compared to past studies and the established knowledge of the electronic structure of MoS_2.

ACKNOWLEDGEMENTS

Thank you to everyone who has supported me in this process, not just for my thesis but throughout my scientific journey so far - for this, I not only have a village but what seems to be an entire city of people to thank. First and foremost, I would like to thank Dr. Clemens Heske for your mentorship and continuing support. For doing something as wonderful as letting a freshman Economics/Mathematics student without prior experience in Chemistry into the lab, changing my entire outlook and career trajectory in the process. For seeing the potential and possibilities that others may not, I could not thank you enough.

A big thank you Dr. Dirk Hauschild and Dr. Lothar Weinhardt for helping me at every step and for your boundless scientific knowledge (and for the jokes). To group members, present and past, thank you for your treasured friendships and fruitful discussions. To the UNLV committee and UNLV administrative staff, thank you for your support.

I would be remiss if I also didn’t thank my friends and colleagues at Brookings Mountain West, the Lincy Institute, and the Brookings Institution – particularly Dr. Carol Graham, Bill Brown, Dr. Caitlin Saladino for your indomitable spirits and mentorship in public policy.

To my family and friends, thank you for being my support system – to Svetlana, Nicole, the Brunch Bunch, the Heske family, you have all made such a positive impact in my life. Fiona and Gidget, for being my emotional support fluffballs during this process. To my parents, thank you for your endless patience and understanding. Finally, to my friends and family in Ukraine, your strength, courage, and resilience will always be inspiring.

TABLE OF CONTENTS

LIST OF TABLES

LIST OF FIGURES

CHAPTER 1: INTRODUCTION

In this work, a 2H phase molybdenum disulfide (MoS_2) single crystal is investigated using a toolchest of spectroscopic techniques in order to uncover its chemical and electronic properties. This material is part of a larger family of transition metal dichalcogenides (TMDC) that have garnered much attention due to its unique and complex electronic and optical character. TMDC's, like MoS_2, are defined by two-dimensional layers composed of S-M-S, where the metal (molybdenum atoms) is sandwiched between two layers of chalcogenides (sulfur atoms). The molybdenum is covalently bonded to the two chalcogen layers, while weak van der Waals forces couple the layers together to form the bulk crystal.[1,2]

MoS_2 has important applications in solar cell devices, batteries, optical sensors, biosensors, electrochemical biosensors, and is even considered a promising electrocatalyst for the hydrogen evolution reactions.[3–5] The material is comparable and offered as an alternative to graphene, which has similar characteristics in its carrier mobility and high structural flexibility.[6,7] One of the most discussed aspects about MoS_2 is its band structure and bandgap that has been reported to change from an indirect bandgap while in its bulk form into a direct bandgap with decreasing number of layers.[8–10]

There are different techniques that have been used to treat the surface of the single crystal or extract individual layers of the MoS_2 through various exfoliation techniques. One of the most straightforward and used techniques is the mechanical exfoliation achieved using adhesive tape.[5,8,11–17]

Despite MoS_2 being an intensely studied material, questions remain concerning the effects of such mechanical exfoliation techniques and what causes the supposed change of the band gap from an indirect to a direct one. Many have speculated quantum confinement effects or spin orbit splitting to be the cause of such a unique electronic structure while others raise concerns over the effects that substrates may have in optical measurements for the single-layered MoS_2.[9–11]

To gain insight about these notable topics concerning MoS_2, lab-based experiments were performed at University of Nevada, Las Vegas (UNLV) and synchrotron-based experiments were performed at the Advanced Light Source (ALS), Lawrence Berkeley National Laboratory. AT UNLV, x-ray photoelectron spectroscopy (XPS) was used to uncover the chemical structure at the surface of the single crystal. In addition, ultraviolet photoelectron spectroscopy (UPS), inverse photoemission spectroscopy (IPES) measurements were also conducted at UNLV and give information about the electronic structure of the MoS_2 crystal surface. This information was then combined with structural information gathered using low energy electron diffraction (LEED). While soft x-ray absorption and x-ray emission spectroscopies have individually been utilized to study TMDCs, the bulk-sensitive resonant inelastic x-ray scattering (RIXS), performed at ALS, offers additional insights, and provides momentum-resolved information about the single crystal. The RIXS technique has the benefit of not being sensitive to surface contaminations and charging effects, qualities that otherwise make it difficult to accurately derive the electronic structure like with angle-resolved ultra-violet photoelectron spectroscopy studies. To aid in the electronic structure discussions, theoretical calculations of the density of states and band structure were also performed using the WIEN2k software package.

The organization of the thesis will be as follows: Chapter 2 will give an overview of the theoretical background and the experimental techniques utilized in this study as well as information about the 2H phase MoS_2 material system investigated. Chapter 3 will discuss the chemical environment of the MoS_2 single crystal surface and how the mechanical exfoliation performed on the surface of the crystal effects its chemical structure. Finally, the corresponding electronic structure of the single crystal, with both lab- and synchrotron-based techniques (primarily RIXS), will be the focus of Chapter 4. Here, the effects of the mechanical exfoliation will also be evaluated in addition to an in-depth discussion about the band dispersion and bandgap values derived from UPS, IPES, and RIXS. These experimental results will be compared to theoretical calculations and established knowledge of the MoS_2 electronic structure.

CHAPTER 2: BACKGROUND

2.1 Introduction

Chapter two presents an overview of the theoretical background and experimental details of the spectroscopic techniques (both lab- and synchrotron-based) utilized in this study and concludes with a discussion on the MoS_2 material system and its relevant electronic properties.

The lab-based experiments utilized in this study were performed at the University of Nevada, Las Vegas (UNLV), and include x-ray photoelectron spectroscopy and x-ray Auger electron spectroscopy (XPS and XAES, respectively), which probe the chemical surface structure. Other techniques include ultraviolet photoelectron spectroscopy (UPS), which yields information about the occupied electronic states and is discussed in tandem with inverse photoemission spectroscopy (IPES) that provides information about the unoccupied electronic states. Low energy electron diffraction (LEED) is also utilized in this study to identify the lattice structure and parameters of the single crystal. For the synchrotron-based techniques, resonant inelastic x-ray scattering (RIXS) was utilized, which combines information from both x-ray absorption spectroscopy (XAS) and x-ray emission spectroscopy (XES). RIXS measurements were performed at Advanced Light Source (ALS) at the Lawrence Berkeley National Laboratory (LBNL).

2.2 Theoretical Background

2.2.1 Lab-based spectroscopic techniques

The photoelectric effect, originally discovered by Heinrich Hertz in 1887 and later theoretically described by Albert Einstein, plays a central role in the photoelectron spectroscopy (PES) techniques utilized to investigate the surface chemical and electronic structure. Generally speaking, this effect involves a photoelectron that is ejected from a sample and into vacuum when photons of a certain energy are incident on the surface.[18–20] The kinetic energy, indicated by E_K, of the ejected photoelectron is given by the following equation:

$$E_K = h\nu - E_B \tag{2.1}$$

Where hv represents the energy of the incoming photon and E_B is the binding energy of the atomic orbital from which the ejected electron originates from.[19] The kinetic energy also includes the work function of the sample, which refers to the minimum amount of energy needed to expel an electron from a solid into vacuum and is the difference between the Fermi energy (E_F) and the vacuum level (E_{Vac}) of the sample. Each element has a unique set of kinetic and binding energies that can be identified in a spectrum, with energies that also correspond to specific chemical environments of that element. Figure 2.1 gives a pictorial description of the various processes for the corresponding lab-based spectroscopic techniques (XPS, XAES, UPS, IPES) and will be used to aid the following descriptions.

As depicted by the purple lines in Figure 2.1, the incoming x-ray photons in XPS excite electrons from a specific core level (CL) into ultra-high vacuum (UHV), which are then detected using a hemispherical electron analyzer. This technique is a powerful tool that can be used to uncover the chemical structure at the surface and give in-depth information about the bonding environment, oxidation states, final state as well as screening effects of the measured sample. This is done by comparing the intensity,

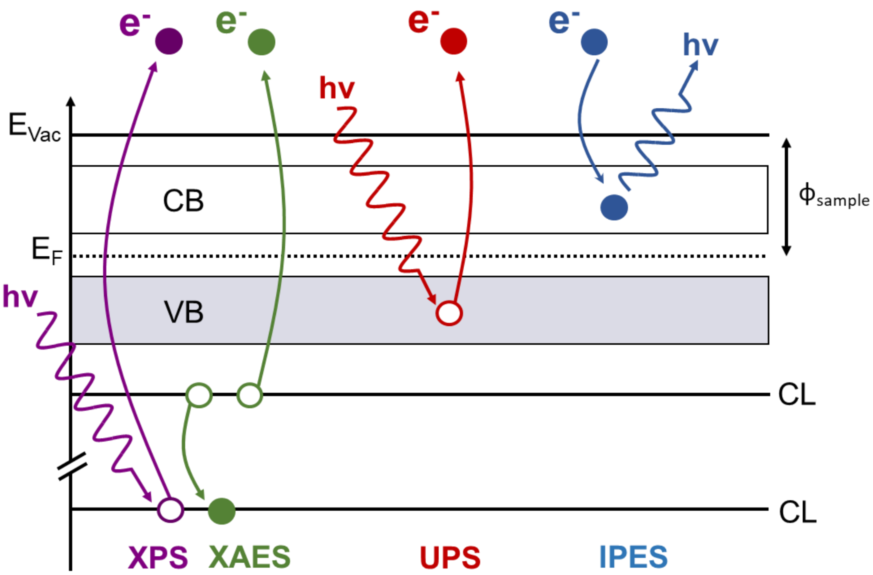

Figure 2.1: Schematic drawing of x-ray photoelectron spectroscopy (XPS, purple lines), x-ray-excited Auger electron spectroscopy (XAES, green lines), ultra-violet photoelectron spectroscopy (UPS, red line), and inverse photoemission spectroscopy (IPES, blue line).

shape, and peak position of the spectral features between different measurement rounds and references. There are several types of satellite features present in the XPS spectra that need to be considered when analyzing a spectrum. Since the x-ray source used in this study is non-monochromated, this means that additional peaks will be present, in smaller intensity, that correspond to photon wavelengths in addition to the main line.[19] Other relevant spectral features in XPS include plasmons and shake-up satellites. Plasmons, which are caused by interactions between the photoelectrons and electrons, can typically be identified by a series of smaller, broader peaks located at higher binding energies after a photoelectron line with peak positions at specific increments in binding energy.[18,19] Shake-up and shake-off excitations can also be present in a XPS spectra and occur when an electron from an inner shell is ejected so fast that the outer shell electrons have no time to relax.[19–21] In a shake-related processes, the ejecting photoelectron and the electrons left behind may interact which can decrease the E_K of the photoelectron and transfer that energy to the system that is then released as shake-up and shake-off contributions.[21]

The surface sensitivity of PES measurements is dictated by the inelastic mean free path (IMFP) of the emitted or incident electrons. Essentially, the longer of a path the electron has to take in a sample, the more likely that electron is to be inelastically scattered. IMFP depends on the kinetic energy of the incident photons and the sample compositions.[20] If an electron is inelastically scattered, it may still be detected by the electron analyzer but may contribute to the background of the measured spectrum and not contribute to the intensity at the correct final state energy.[20] As will be seen in Section 3.2.1, the overall background of the survey spectrum increases with increasing binding energies (or lower kinetic energies), which is a result of inelastic scattering processes that create secondary electrons that are detected at higher binding energies.[19,20]

XAES peaks are also observed in the XPS spectra and correspond to a process where a second electron is ejected. The Auger process, as depicted by the green lines in Figure 2.1, is a secondary, non-radiative process in which an electron from a higher energy level relaxes into a core hole in at a lower energy level that was created from the first ejected photoelectron. In order to conserve the energy difference between the two core levels, a second electron is ejected and produces a peak that is typically broader than the photoelectron lines. The spectra derived from XPS is typically plotted with intensity (arbitrary units) as the ordinate and binding energies as the abscissa. For XAES, the energy axis of the Auger regions is plotted in kinetic energies since Auger emission is independent of the excitation source.

UPS provides information about the occupied density of states below Fermi energy (E_F), as shown by the red lines in Figure 2.1. This technique allows for the measurement of the valence band region, d-band states, and the secondary electron cut-off (from which the work function can be derived using linear extrapolation). This technique gives the total density of states integrated over all k-points of a single crystal. From the valence band measurements, the leading band edge can be derived using linear extrapolation. XPS can also be used to probe the valence band region, however this technique does not have as high of flux or narrow-line widths as UPS He I and He II excitation energies do in the valence band region.[20] UPS can then be paired with its complementary techniques of inverse photoemission spectroscopy (IPES), an electron-in and photon-out process that probes the unoccupied density of states above the Fermi energy. As seen in Figure 2.1, indicated by the blue line, a beam of low energy electrons bombards the surface of the sample, allowing for electrons of a certain energy to relax into unoccupied states within the conduction band.[22] This relaxation produces an emission of a photon that is then detected by an IPES detector (in this study, a photomultiplier tube). The electron source scans through a range of electron energies while the photon energy is held constant. The energy of the emitted photon corresponds to an energy of E_i – E_f and is representative of the available electronic states in the conduction band.

From UPS, the valence band maximum (VBM) can be combined with the conduction band minimum (CBM) from IPES to find the electronic surface bandgap of the material, which is done by linearly extrapolating the leading band edges of the spectra.[23,24] Linear extrapolation is a suitable method of deriving the uppermost electronic states of the valence band since valence band spectra shown here are integrated over k-space. Additionally, non-symmetric broadening as a result of limited angular resolution of the electron analyzer (for UPS) or the electron gun (for IPES), inelastic scattering processes, and incomplete screening may lead to shifts of bands to higher binding energies.[23–25] This method gives a good description of the VBM and CBM at the high-symmetry-point of the crystal in momentum space, which will be positioned at the inner bounds of VBM and CBM (closer towards the E_F). While for semiconductors, UPS and IPES provide the bandgap value, for metals, which do not have a bandgap, the techniques give a measurement of the Fermi edge. This Fermi edge is used to derive the Fermi energy and set as the relative energy for comparisons between UPS and IPES measurements. For XPS and UPS, because the techniques result in an ejection of an electron, the system is left with an N – 1 electronic configuration while for IPES, the system is left with an N + 1 configuration because of the additional electron. Further information about the lab-based spectroscopic techniques is available in references [18] and [20].

The spectrum for each of these techniques is dictated by the probability of a specific transition per unit of time, which can be described using Fermi's Golden Rule (as described in ref [26]):

$$P_{i\to f} \propto |\langle f|\widehat{H_P}|i\rangle|^2\, \delta(E_f - E_i \pm h\nu) \tag{2.2}$$

In the time-dependent first order perturbation theory, $P_{i\to f}$ gives the probability of a transition for the initial state (i) to the final state (f) by a perturbation operator. The initial and final states are different between the spectroscopic techniques: with PES, the initial state is typically the ground state. The final state is a free electron and a core hole for XPS, or a free electron and a valence hole for UPS. The transition matrix element is given by $\langle f|\widehat{H_P}|i\rangle$ derived by P.A.M. Dirac in 1927.[26] The δ function accounts for energy conservation. The "minus" in the δ function refers to an absorption process, while the "plus" describes the emission process. Disregarding multi-photon processes and applying the dipole approximation that assumes a constant electric field over the spatial variation of the electron wave function,[27] an simplified expression is:

$$P_{i\to f} \propto |\sum_k \langle f|\hat{e}x_k|i\rangle|^2\ \delta(E_f - E_i \pm h\nu) \tag{2.3}$$

Where ê stands for the unit vector, while x_k refers to the linear momentum operator of the electrons.

2.2.2 Synchrotron-based spectroscopic techniques

Soft x-ray photon-in-photon-out techniques were also utilized in this study, specifically resonant inelastic x-ray scattering (RIXS). Since RIXS combines information from both XAS and XES, the non-resonant XAS and XES will be discussed first to introduce the RIXS process. A basic pictorial description of the three synchrotron-based techniques is available in Figure 2.2, with XAS shown by the red lines, XES shown by the blue, and RIXS shown by the purple lines. In the non-resonant XAS and XES case, the description of the process differs from the RIXS process and is instead viewed as an "absorption followed by emission" process.[28] As indicated by the XAS schematic in Figure 2.2, incident photons can be tuned to an energy for which an electron from a core level is excited into an unoccupied state in the conduction band. Afterward, an electron (typically from the valence band) relaxes into the core hole and a photon is emitted, as indicated by the XES schematic depiction in Figure 2.2.

Soft XAS is a photon-in-photon-out process that probes the unoccupied density of states by measuring the probability of an x-ray photon being absorbed as a function of photon energy. As mentioned with the PES techniques, the probability of a specific transition per unit of time can be described using Fermi's Golden Rule. The intensity of XAS spectra can be expressed by integrating Equation 2.4 over all possible final states while also accounting for energy conservation (according to ref [29]):

$$I_{XAS}(h\nu_{in}) \propto |\sum_k \langle f|\hat{e}x_k|i\rangle|^2 \, \rho\left(E_f\right) \, with \; E_f = E_i + h\nu_{in} \qquad (2.4)$$

The $\rho(E_f)$ describes the density of states (DOS). Here, the initial state is also the ground state, like with PES, but is a combination of an excited electron and a core hole in the final state.[30] The complimentary technique to XAS is XES, which is also a photon-in-photon-out process, but one that probes the *occupied* density of states by measuring the emission probability as a function of emission energy. XES intensity can be expressed as follows:

$$I_{XES}(h\nu_{out}) \propto |\sum_k \langle f|\hat{e}x_k|i\rangle|^2 \, \rho(E_i) \, with \; E_i = E_f - h\nu_{out} \qquad (2.5)$$

The initial state for XES is the core hole system, while its final state contains a valence hole.[30] The dipole transition matrix element dictates that only states fulfilling specific symmetry and dipole selection rules are allowed to be probed, i.e., that $\Delta l = \pm 1$. The overlap of states and core level orbital determines the intensity contributed to a spectrum,[31] meaning that the local density of states at a specific atomic species is probed with XAS and XES. Probing the local electronic (and thus also chemical) environment is a clear distinction of XAS and XES compared to PES.[31] The valence hole influences the XES spectral contributions, while the XAS spectrum is influenced by the core hole effects in its final states.[32]

In the resonant excitation regime, the emission spectra have a strong dependence on the excitation energy, an effect that was first described by Rubensson et al.[33] While non-resonant XAS and XES can be approximated well enough as separate steps, the RIXS process needs to be describes strictly as a one-step scattering process.[31,34,35] To do this, Fermi's Golden Rule needs to be replaced by the Kramers-Heisenberg formalism to properly describe the resonant effects.[36] The intensity of the RIXS process is given as:

$$I_{RIXS}(h\nu_{in}, h\nu_{out}) \propto \sum_f \sum_i \frac{|\langle f|p\cdot\hat{e}_{out}|m\rangle\langle m|p\cdot\hat{e}_{in}|i\rangle|^2}{(E_m - E_i - h\nu_{in})^2 + \Gamma_m^2/4} \cdot \delta(h\nu_{in} - h\nu_{out} - E_f + E_i) \qquad (2.6)$$

Here, the resonant term involves the initial and final states, as well as an intermediate state m. The first-order perturbation that was used for non-resonant XAS and XES now requires second order perturbation theory, which is expressed by the Kramers-Heisenberg formulism that was modified by Weisskopf and Wigner in order for intermediate states to have finite lifetimes instead of infinite ones.[27,37] The summation terms imply that the scattering intensity is determined by the amplitude of the absorption and emission process rather than their probabilities.[31] The δ function determines the energy of the emitted photon, while the incoming photon energy can be detuned within Γ_m, which refers to the lifetime broadening of the intermediate state m. The contributions of the resonant and non-resonant states depend on the lifetime width of Γ_m and it is possible to have an on-resonance case, where $|E_m - E_i - h\nu_{in}| \leq \Gamma_m$.[27,35] As shown by the RIXS schematic in Figure 2.2, the final-state electron-hole pair is delocalized, which allows the band dispersion to be measured, as will be elaborated in Section 2.2.3.[32] A RIXS measurement produces a two dimensional color-coded map and will used in this thesis to discuss the electronic structure of 2H phase MoS_2 single crystal.

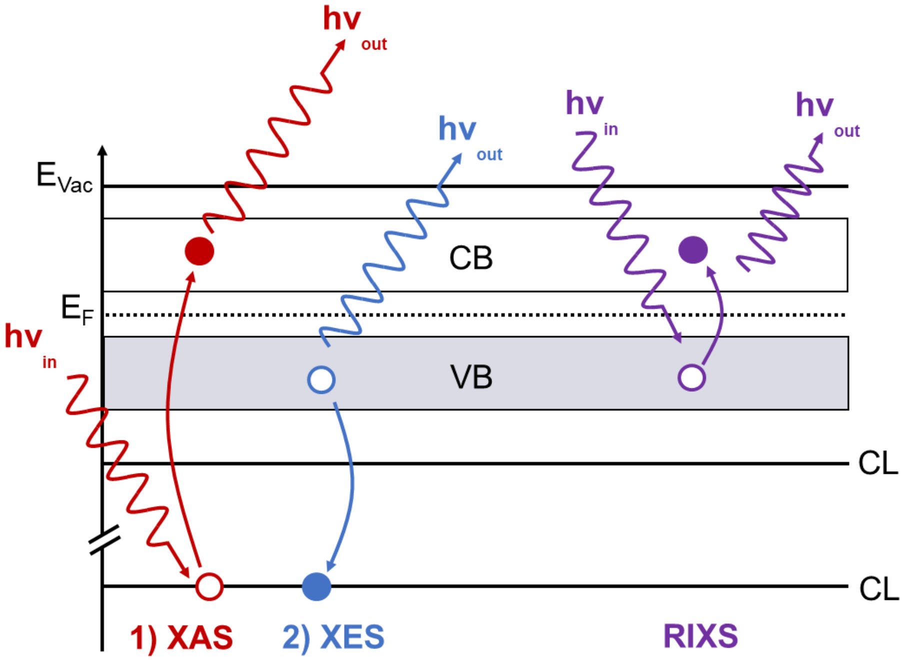

Figure 2.2: Schematic drawing of x-ray absorption spectroscopy (XAS, red lines) and x-ray emission spectroscopy (XES, blue lines) versus the resonant inelastic x-ray scattering (RIXS, purple lines) process.

2.2.3 Probing the crystal momentum

In addition to providing energy-resolved information, it is possible for PES techniques to also be momentum-resolved. Making it possible to experimentally derive the band structure of a crystalline material that make-up the conduction and valence band, and hence give important insights about the electronic structure of the material. In most cases, the crystal momentum is probed using angular-resolved PES (ARPES) techniques that can be carried out in both laboratories and synchrotron facilities. There are many challenges presented with measuring ARPES, as this technique is sensitive to any surface contaminations, and the sample rotation can modify the photoemission matrix elements, polarization geometry, or beam position incident on the sample.[38,39] In this study, since the RIXS process is a photon-in-photon-out technique, the true bulk properties are probed and not influenced by surface contaminations. While techniques like ARPES are sensitive to surface contamination, RIXS is largely insensitive to surface contaminations, as well as sample charging, external electric or magnetic fields, element specific and angular momentum resolution.[28]

In RIXS, momentum conservation is due to the delocalization of the electron-hole pair in the final state.[32] The k-space relationship between the valence hole and the conduction electron is vertical, i.e., along the same value in k-space. The momentum of the electron-hole pair equals the difference between the change of the incident and emitted photons.[28,32] In addition to energy conservation, the δ function in equation 2.6 also means that only k-conserving processes have a nonvanishing cross section.[35] The momentum of the incoming photons is small compared to the extent of the Brillouin zone in the soft x-ray region, as used in this study.[28,31,35]

2.2.4 Low energy electron diffraction

LEED was utilized in this study to verify the crystal surface structure of the single crystal. In LEED, low-energy electrons are scattered from the surface and can be used to study the geometric positions of surface atoms.[40] For this technique, a beam of monochromatic electrons of low energies (typically below 150 eV) are diffracted (back-scattered) by the surface of a crystal and can be focused with a lens system and grid.[41,42] These incident electrons are elastically scattered and are detected by a fluorescent screen with patterns that represent the diffraction pattern in reciprocal space. This technique is surface sensitive (substantially more so than classical x-ray diffraction) and is strongly affected by even a small amount of surface impurities.[20,42]

2.3 Experimental Details

2.3.1 Lab-based measurements

The lab-based experimental techniques were performed in a multi-chamber ultra-high vacuum system at UNLV. For XPS measurements, a non-monochromated Specs XR 50 x-ray source with Mg K_α and Al K_α anodes (photon energies 1253.6 and 1486.6 eV, respectively) was employed.[19] Cu, Au, and Ag foils were cleaned using Ar^+ ion sputtering and used to calibrate the XPS spectra according to reference [19]. UPS measurements were conducted using a monochromated He I and II (hv ≈ 21.2 and 41.8 eV, respectively) with a Gammadata VUV 5000 source. A bias voltage of approximately 18.8 V was applied to the grounded sample to separate the secondary electron cut-off and the rest of the valence band features from the work function of the electron analyzer and was accounted for in the energy calibration. For both of these techniques, a Scienta R4000 hemispherical electron analyzer was used to detect the ejected photoelectrons. UPS valence band spectra were combined with IPES, which was measured using a STAIB NEK-150-1 low-energy electron gun. The emitted photons were then detected with a Hamamatsu R6834 photomultiplier tube and a Semrock Hg01-254-25 mercury line filter detector window (with a central photon energy of 4.88 eV derived using UV-Vis spectroscopy).[43] A silver foil was cleaned using Ar^+ ion sputtering and measured with both UPS and IPES to find the Fermi edge. This Fermi edge was then used to calibrate the energy scale of both UPS and IPES measurements and for determining the overall energy resolution, ~115 meV for UPS and ~420 meV for IPES. An Omicron SPECTALEED rear-view LEED was used to verify the lattice structure of the crystal surface. A bias voltage of ~60 eV was used to find the pattern of the exfoliated sample.

2.3.2 Synchrotron-based measurements

At the Advanced Light Source (ALS) at Lawrence Berkeley National Laboratory, an as-received 2H phase MoS_2 single crystal was measured with RIXS at Beamline 8.0.1. The excitation and emission energy scales were calibrated using reference measurements and literature values for boron nitride and $CaSO_4$. To collect the data, the Variable Line Spacing (VLS) spectrometer installed at the Solid and Liquid Spectroscopic Analysis (SALSA) end station was used.[44]

2.3.3 Density functional theory calculations

To aid in the discussion of the electronic structure of MoS_2, density functional theory calculations were performed using the WIEN2k program package. Particular focus was placed on the analysis of the density of states and band structure. WIEN2k is based on the full-potential augmented plane wave plus local orbitals (APW + lo) method to solve the Kohn-Sham equations.[45] Here, a 5,000 k-point mesh was used for total and partial density of states (PDOS), and XES calculations. The generalized gradient approximation (GGA) as parameterized by Perdew, Burke, and Ernzerhof (PBE) was used to describe the electronic exchange-correlation functional.[46] The 2H phase MoS_2 crystal structure information was gathered from the Materials Project Database (material ID mp-2815); calculations were performed for a space group of $P6_3/mmc$ and a selected k-path of Γ-K-M-Γ.[47,48]

2.4 Material System

2.4.1 Transition metal dichalcogenides

Transition metal dichalcogenide (TMDC) refers to a class of materials characterized by a layer of transitional metal atoms (namely Mo, W, and Ta) that are covalently bonded to two layers of chalcogenide atoms, e.g., S, Se, and Te. There are over 60 types of TMDC structures, most of which have a layered structure, with layers stacked together to form a bulk crystal structure.[1,49] These stacked layers are held together by weak van der Waals forces what make it easy to separate the individual layers. Two-dimensional TMDC have been found to have high thermal conductivity and optical transparency.[1,13] How the metal and chalcogenide atoms are stacked within a layer has a direct impact on its electronic properties according to previous studies. For example, if the two chalcogenide atoms are positioned directly above each other, the TMDC forms a trigonal prismatic structure, otherwise an octahedral structure forms when the chalcogenide atoms are slightly slanted in their position.[50] TMDC have an incredible range of applications in energy conversion devices like thin-film solar cells, as well as batteries, bio-sensors, flexible electronics, DNA sequencing and personalized medicine.[6] Moreover, two-dimensional TMDCs like WSe_2 have been used as absorbers to create ultrathin devices that have efficiencies of up to 5.1% while other TMDCs have been integrated within perovskite solar cells to improve their stability.[51,52] One of the most prominent and studied TMDC materials is MoS_2, which was first described by Roscoe G. Dickinson and Linus Pauling in 1923.[53]

MoS_2 is also often discussed as an alternative to graphene, which is viewed as a gap-less material with similar characteristics as MoS_2 in its carrier mobility and flexibility.[6,7,54] As a result, it has also been suggested to be used in tandem with graphene for highly flexible and transparent transistors.

2.4.2 Synthesis and exfoliation techniques

MoS_2 single crystals are often synthesized using chemical vapor transport, but the synthesis of these crystals can be separated into two types of methods, top-down or bottom-up approaches.[1,5,54,55]

There are also several prevalent mechanical and chemical exfoliation techniques used with this material to either clean the surface of the crystal from adsorbates or extract individual layers. Mechanical exfoliation using adhesive tape is a common technique implemented for transition-metal chalcogenides to transfer single layers or remove surface adsorbates from the crystal.[5,8,11–17] In this study, once the tape was placed onto the crystal, equal pressure was applied to ensure that a maximally large-area piece of the MoS_2 layer would be removed.[15] The exfoliation was performed multiple times to remove several layers from the surface. Although each layer peeled off easily, they were uneven and resulted in a surface that was not completely flat on the macroscale (but, presumably, flat on the nano-, if not even micro-scale). In previous studies, this exfoliation method gave only small flakes of MoS_2 and was not deemed feasible for large-scale exfoliations**.**[4] Liquid-phase exfoliation based on organic solvents is seen as a more scalable alternative to mechanical exfoliation that also allows for layers of controllable thickness to be exfoliated.[56] However, this method of exfoliation, which relies on Li intercalation, has been shown to modify the phase of the MoS_2 single crystal.[3,4,6]

2.4.3 2H versus 1T versus 3R phases of MoS_2

In its bulk form, the MoS_2 structure can be a hexagonal (H), triagonal (T), and rhombohedral (R) crystal system, each comprising of a different stacking scheme of the Mo and S atoms. There three main structures MoS_2 is present in are 2H, 1T, and 3R – the numbers in front of the letter refer to the number of layers present within that crystal system.[5] In the 1T structure, the S plane is shifted, and the S atoms and the two layers are no longer directly above one another.[4] 2H acts like a semiconductor (and has poor capability of charge transfer), while 1T acts more metallic.[3,4] The 2H phase MoS_2 is the thermodynamically stable crystal structure, while 1T is unstable without additional electron injection.[4]

2.4.4 Crystal structure of 2H MoS_2

Figure 2.3 shows the 2H phase crystal structure, as modelled in the VESTA visualization program from both the top and side of the structure.[57] The sulfur atoms are indicated by the yellow spheres, while the purple spheres represent the molybdenum atoms. 2H phase MoS_2 crystal structure information was gathered from the Materials Project Database (material ID mp-2815).[47] Figure 2.3 also shows the Brillouin zone of the crystal and the relevant high-symmetry points. The 2H MoS_2 hexagonal Bravais lattice translates into a hexagonal first Brillouin zone when transformed from real to reciprocal space.[7,58] The Γ point represents the center of the Brillouin zone (and is not to be confused with the lifetime of the intermediate state in RIXS), and the M and K point represent the other high symmetry points of the structure.[18]

The band structure of the bulk 2H phase MoS_2 is depicted in Figure 2.4, calculated as described by the procedure in Section 2.3.3, with an energy axis relative to the VBM.

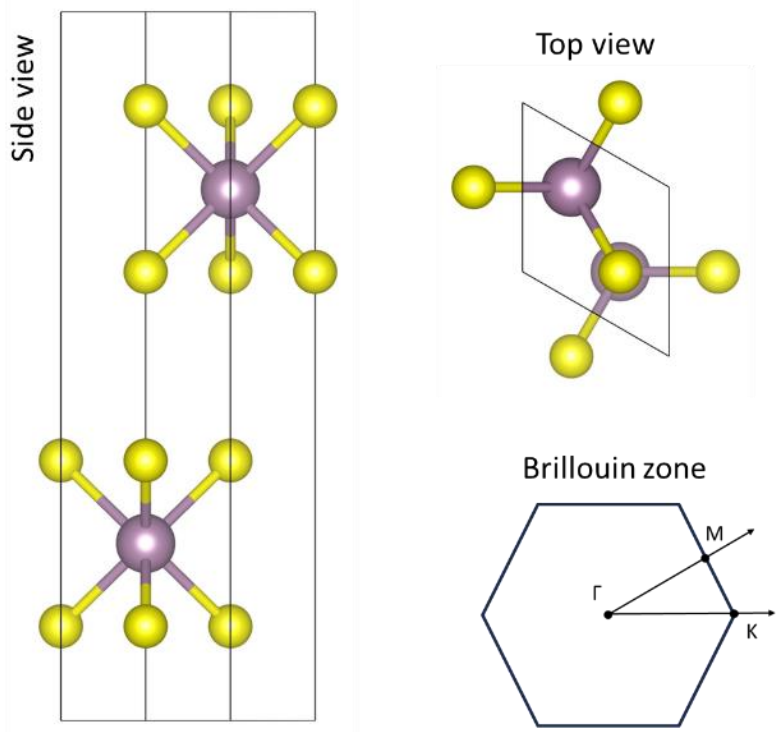

Figure 2.3: Diagram of the 2H phase MoS_2 crystal structure from a top (right) and side view (left) using the VESTA visualization program. Yellow spheres represent the S atoms and the purple spheres represent the molybdenum atoms. The top view of the Brillouin zone of the crystal is also shown (bottom right).

The red line highlights the topmost valence band and the blue line highlights the lowermost conduction band along the Γ-K-M-Γ k-path. Most of the contributions in the two lowermost bands of the conduction band between the Γ and K points, as well as the Γ and M points, can be attributed to the Mo $d_{x^2-y^2,xy}$ orbitals, while a linear combination of delocalized Mo d_{z^2} orbital and antibonding S p_z orbitals contribute around the K and M points. The states near the Γ point in the valence band are also predominantly derived from a linear combination of delocalized Mo d_{z^2} orbital and antibonding S p_z orbitals. S p_x, p_y, and p_z, orbitals strongly contribute to the bands positioned around -6 eV between the M and Γ points, with some contribution from Mo $d_{x^2-y^2,xy}$ and Mo d_{z^2} as well.

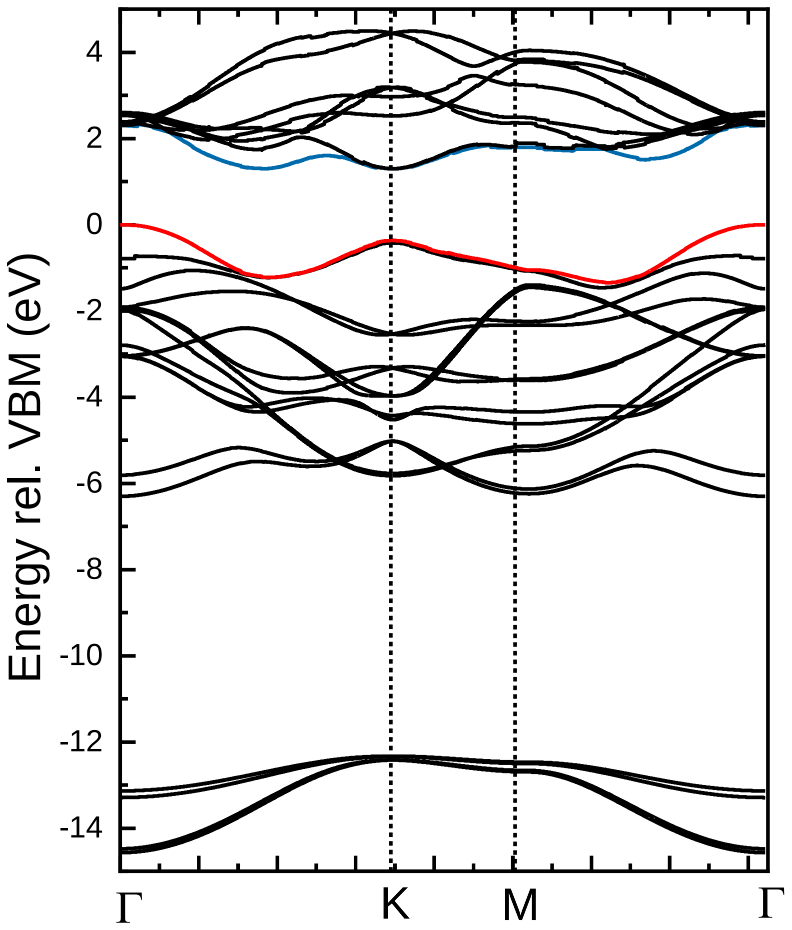

Figure 2.4: Calculated band structure of 2H phase MoS_2 with the VBM values set at zero eV. The topmost valence band is indicated by the red line and the bottommost conduction band is indicated by the blue line.

CHAPTER 3: CHEMICAL ENVIRONMENT OF 2H MOS$_2$ SINGLE CRYSTAL

3.1 Experimental Details

To study the properties of 2H phase MoS$_2$, a single crystal was purchased from 2D Semiconductors. At their facilities, the single crystal was synthesized via chemical vapor transport.[55] At UNLV, the single crystal was transferred and stored in a glovebox filled with inert nitrogen gas where it was unsealed from its packaging, mounted onto a sample plate, and introduced into the ultra-high vacuum system. The crystal, 15 x 7 x 1 mm^3 in size, was first measured with XPS using non-monochromated Mg and Al K$_\alpha$ from a Specs XR 50 x-ray source and a Scienta R4000 electron analyzer. Cu, Au, and Ag foils were cleaned using Ar$^+$ ion sputtering and used to calibrate the XPS spectra according to reference [19].

The single crystal was initially measured “as-received,” without any surface treatment or exfoliation. Afterwards, the crystal was transferred back into the glovebox and mechanically exfoliated using the adhesive tape method.[5,8,11–17] The mechanical exfoliation was performed multiple times to remove several flat layers from the surface in hopes of removing surface adsorbates. Although each layer peeled off easily, the peels were uneven and resulted in a crystal surface that was not completely flat. This creates challenges with angular resolved photoelectron measurements,[59,60] however the data presented in this chapter is integrated over k-space.

Finally, LEED was performed on an exfoliated sample using the Omicron SPECTALEED rear view LEED in order to verify the lattice structure of the crystal surface. The exfoliated single crystal was analyzed with LEED using a ~60 eV bias voltage.

3.2 Results and Discussion

3.2.1 Effects of mechanical exfoliation on a MoS_2 chemical surface structure

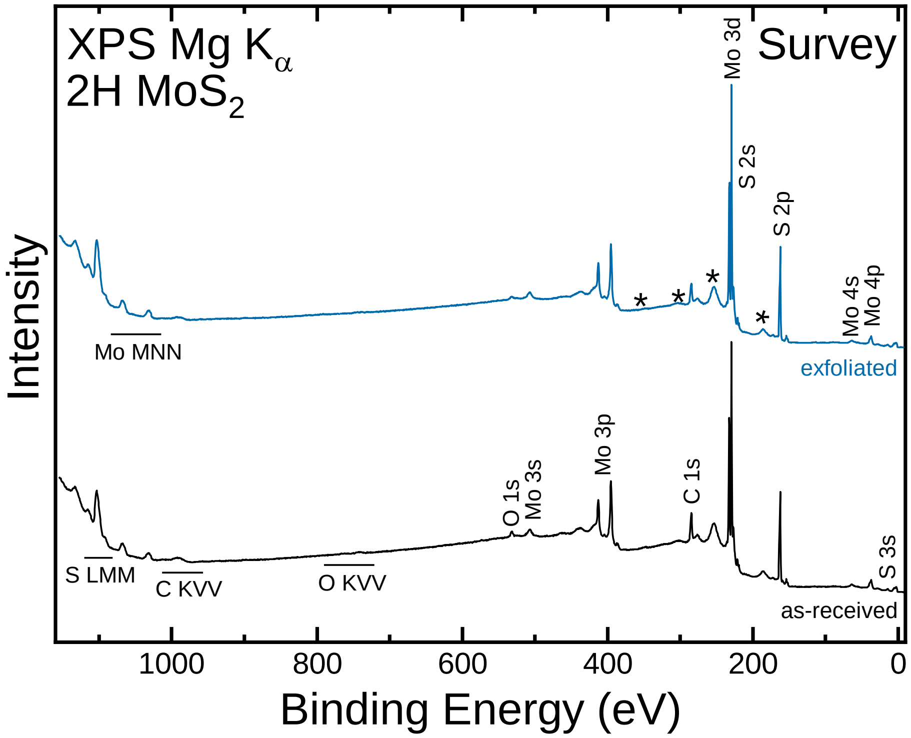

Figure 3.1: XPS Mg K_α surveys of the as-received (black) and exfoliated (blue) 2H phase MoS_2 single crystal with prominent photoelectron and Auger features labelled. Asterisks (*) refer to loss features for molybdenum and disulfide photoelectron lines, respectively.

An overview of the surface chemical structure using the XPS Mg K_α survey spectra of both the as-received (black line) and exfoliated (blue line) 2H phase MoS_2 single crystal is shown in Figure 3.1. All relevant photoelectron and Auger peaks are labelled (i.e., for Mo and S), along with associated contaminants like oxygen and carbon. Both surveys show high-intensity Mo-related peaks, and lower-intensity S-related peaks (the lower intensity being due to photoionization cross section effects). Both carbon and oxygen signals are found, with greater as-measured signal intensity of the C 1s peak compared to the O 1s. After exfoliation, O- and C-related peaks decrease in intensity, but are not completely removed, while Mo- and S-related peaks increase in intensity. The asterisk (*) refers to energy losses (e.g., bulk plasmons) for MoS_2 photoelectron lines.[20,61,62]

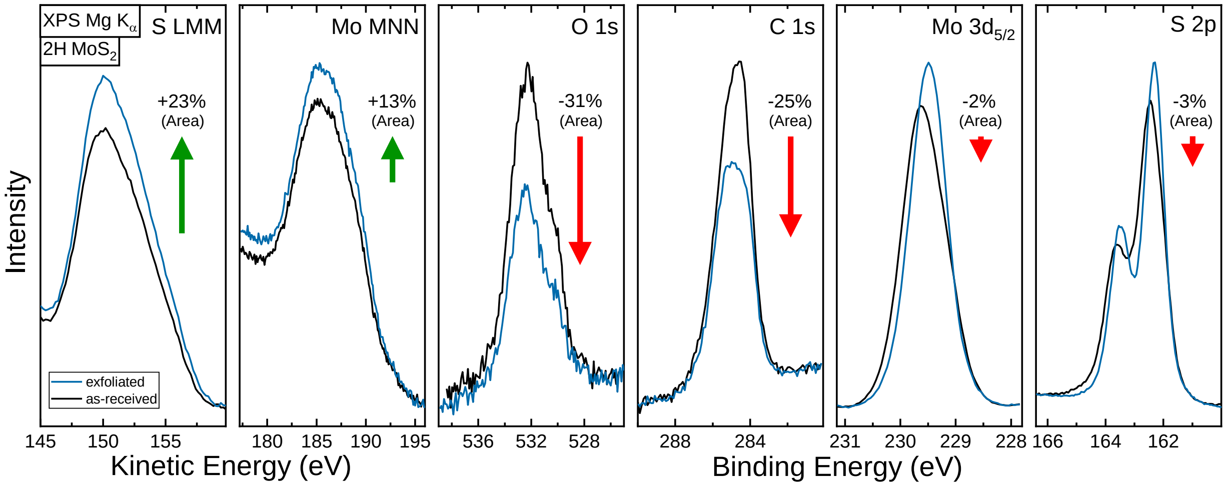

Figure 3.2: Detailed Mg Kα XPS spectra of S LMM, Mo MNN, O 1s, C 1s, Mo $3d_{5/2}$, and S 2p regions for both as-received (black) and exfoliated (blue) sample surfaces. Arrows indicate the relative changes of the area under the peaks of the exfoliated sample, compared to the as-received sample.

The changes in the shape and intensity between the as-received and exfoliated surfaces can be more clearly seen in the detailed spectra shown in Figure 3.2. To have a clearer comparison, the peaks have been shifted vertically to have matching background at higher kinetic energies/lower binding energies. When comparing the area of a peak from the as-received surface to the exfoliated surface, a decrease of 31% is seen in the area of O 1s (indicated by the red arrow in the plot), and a smaller decrease of 25% is derived for the C 1s area. While the intensity of both the Mo $3d_{5/2}$ and S 2p peaks increase, the area remains similar, since the shoulders of the as-received peaks are broader. Meanwhile, the area of the corresponding Augers lines for both S and Mo increased, 23% for S $L_{23}M_{23}M_{23}$ and 13% for Mo $M_{45}N_{23}N_{23}$. This could be the result of changes in the steep background seen at lower kinetic energies, as well as the removal of adsorbates that would affect peaks at the lower kinetic energies more due to shorter inelastic mean free paths.

While the intensity and area of the C 1s peak decreased after exfoliation, it was not completely removed. Looking back at Figure 3.1, it appears that the carbon intensity on the crystal surface is not substantial, even before exfoliation. However, peaks like the Mo 3d have greater photoionization cross-sections compared to the C 1s peak and will have higher intensity in the measured spectra. Figure 3.3 compares the C 1s peak with the Mo $3d_{3/2}$ peak, before and after accounting for differences in the photoionization cross-sections (σ), as well as differences caused by the analyzer transmission function (T) and the inelastic mean free path (λ) of the emitted electrons.[20,63,64] The two left-hand plots show the as-received regions with the as-measured C 1s and Mo $3d_{3/2}$ peaks shown in the solid line, while the readjusted Mo$3d_{3/2}$ peak is shown in a dashed grey line. Similarly,

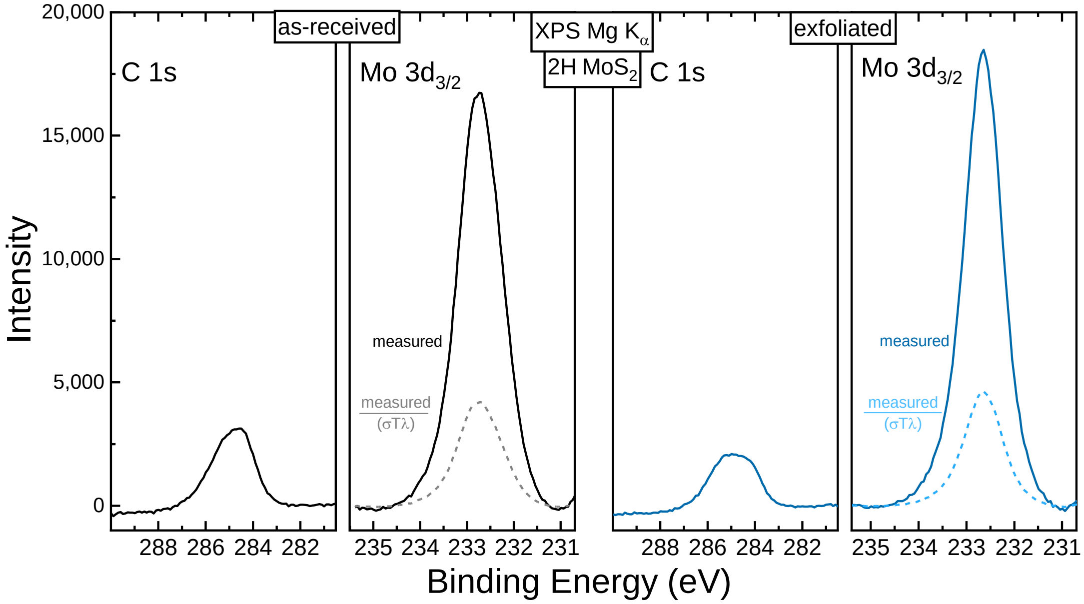

Figure 3.3: C 1s and Mo $3d_{3/2}$ XPS Mg K_α spectra of as-received and exfoliated surfaces, comparing the intensity of the Mo $3d_{3/2}$ emission before (solid lines) and after (lighter dashed lines) relative to the C 1s peaks, considering photoionization cross-sections, transmission function, and inelastic mean free paths.

the two right-hand plots show the corresponding C 1s and Mo $3d_{3/2}$ regions for the exfoliated sample, with the lighter blue dashed line representing the adjusted peak. The photoionization cross sections utilized for these readjustments were calculated by J.H. Scofield using the single-potential Hartree-Slater atomic model with the cross sections of C 1s peak set to 1.00 (in 22,200 barns units).[64] Since the photoionization cross-section of the Mo $3d_{3/2}$ is much larger (3.97) than for the C 1s peak, it has the greatest effect in the intensity adjustment of the Mo peak, while the inelastic mean free path and analyzer transmission are very similar between the two regions. In Figure 3.3, the background for each peak is set to zero and all four plots are set to the same intensity scale. After accounting for σ, λ, and T, the intensity of the Mo $3d_{3/2}$ region is now at similar intensities as the C 1s peak intensity, indicating that carbon and Mo show a similar amount at the surface. After exfoliation, the difference in intensity between the C 1s and Mo $3d_{3/2}$ is more apparent, but carbon is still prevalently detected.

For further quantification, the Mo/C ratio can be derived using the area of the C 1s and Mo $3d_{3/2}$ peaks and the photoionization cross-section, analyzer transmission functions, and inelastic mean free path differences discussed earlier (the equation for the derived ratio is given in Appendix A). The Mo/C surface ratio is found to be 0.71 ± 0.02 for the as-received round, which increased to 0.91 ± 0.02 after the exfoliation. The pervasiveness of carbon suggests that although some of the signal is due to possible air exposure during the sample packing or synthesis process, the carbon is not only an adsorbate but part of the MoS_2 bulk.[65] Other studies show a much larger signal of C 1s on the surface of MoS_2 films, hence in such cases the surface is far more carbon rich.[66–70] For applications in electrocatalytic activity for the hydrogen evolution reaction, a carbon-based MoS_2 was beneficial for increased electrochemical activity.[71–74] For the study here, the presence of carbon and other elements not related to MoS_2 are important to consider during later discussions regarding the electronic structure of the material.

The same analysis can be done for other prevalent elements found on the surface of the MoS_2 crystal, like sulfur (expected) and oxygen (adventitious). Using the area of the S 2p and Mo $3d_{3/2}$ regions, a S/Mo surface ratio of 2.28 ± 0.05 was found for the as-received sample, which decreased slightly to 2.20 ± 0.05 after the exfoliation. The derived ratios before and after the exfoliation are both higher than previously reported S/Mo ratio of 1.92 with a 2H MoS_2 surface.[75] This suggests the possible presence of molybdenum vacancies within the single crystal, which is different from previous studies that identified the formation of sulfur vacancies after annealing a MoS_2 single crystal.[75,76]

A O/C ratio was found at 0.17 ± 0.02 (using O 1s and C 1s peaks) for the as-received sample and decreased to 0.13 ± 0.02 after exfoliation. Finally, the S/C ratio is found to be 1.62 ± 0.05 for the as-received sample and after the exfoliation, increased to 2.00 ± 0.05. Taking all four of the prevalent elements into account, the surface stoichiometry of the as-received MoS_2 is found to be C : O : Mo : S = 29% : 5% : 20% : 46%, and was modified to a surface stoichiometry C : O : Mo : S = 25% : 3% : 22% : 50% after mechanical exfoliation was performed. Overall, sulfur comprises the largest portion of the surface stoichiometry while carbon and molybdenum are at very similar proportions.

To evaluate the changes in the chemical species before and after the exfoliation, Figure 3.4 shows the C 1s and O 1s Mg K_α XPS detailed regions. The intensity is normalized to the maximum peak height for both regions, with literature values of corresponding chemical environments of carbon and oxygen represented with gray boxes above the spectra.[19,65,77–81] The normalized C 1s peak of the as-received sample has a different peak shape compared to the exfoliated sample but is positioned at similar binding energies. The C 1s peak is broader by the peak maximum for the exfoliated surface while being narrower at the shoulders, at both higher and lower binding energies with a lower background at higher binding energies. The decrease in the background at higher binding energies for both the C and O 1s is likely due to the decrease of adsorbate signal and a corresponding decrease in background caused by inelastically scattered electrons. The chemical environment of the C 1s peak is likely a combination of carbon, hydrocarbons, carbon bonded to sulfur, and carbon bonded to molybdenum.[19,65,77–80] The

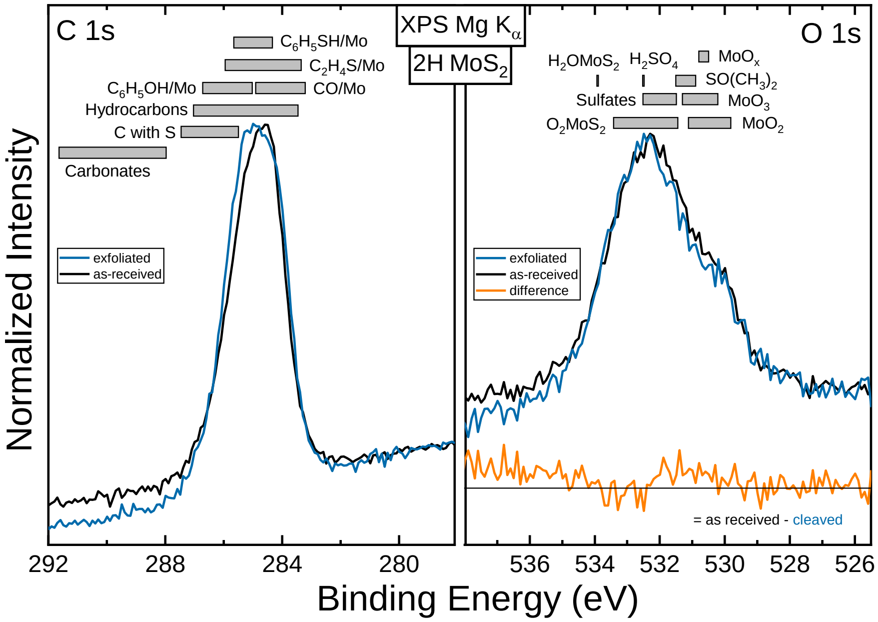

Figure 3.4: Mg K_α excited XPS spectra of C and O 1s, before and after the exfoliation, with literature values for different chemical species represented by gray boxes.[19,65,77–81] All spectra were normalized to the maximum peak height and the difference between the as-received and exfoliated O 1s is also shown (orange line) on the right plot.

normalized O 1s region shows an overall similar shape between the two rounds, with the exception of the binding energy regions around 534 eV as well as between 532 and 529 eV. The orange line at the bottom of the right-hand plot shows the difference between the two spectra, indicating at least one additional species present in the as-received sample. This additional component may correspond to sulfates, $Mo(O_xS_y)_2$, or hydroxides.[19,77,78,80,81]

The S 2p region can give more noticeable indication of the effects of the exfoliation, as the S atoms are, as an overall ensemble, in different environments before and after the exfoliation. As seen in Figure 3.5, the left-hand plot shows two normalized S 2p

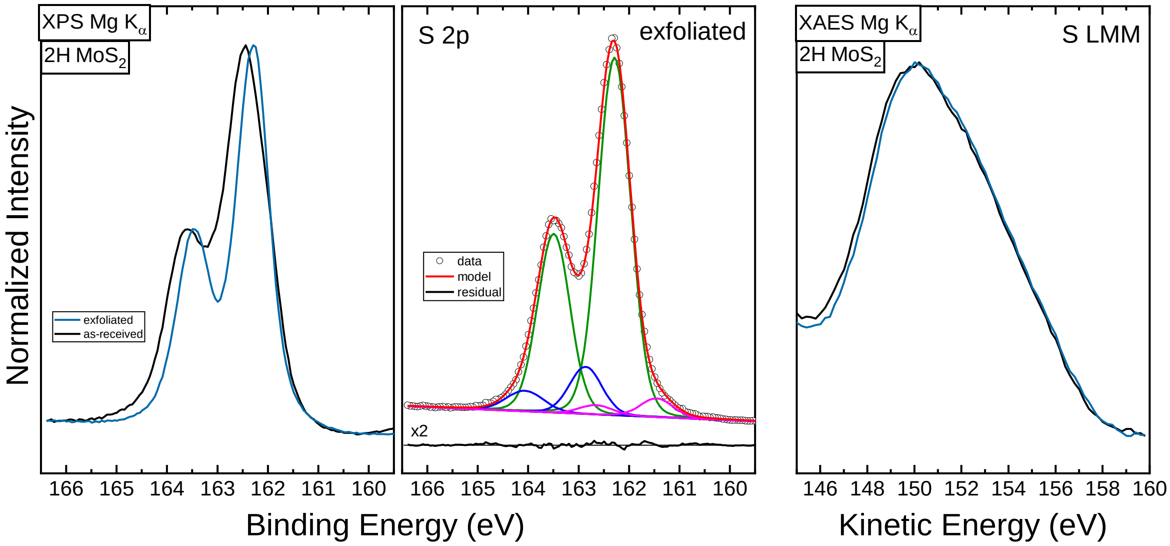

Figure 3.5: Mg Kα-excited S 2p and S LMM spectra with normalized intensities to the peak maximum height for both the as-received and exfoliated measurement rounds. The plot in the center corresponds to a fit of the S 2p region for the exfoliated sample. Raw data is represented with black open circles, while the sum model is shown as a red line and the components are shown as green, blue, and pink lines.

regions corresponding to the as-received and exfoliated samples. After the exfoliation, the S 2p line shifts by -0.18 eV, with the shoulders narrowing at both lower and higher binding energies. The “valley” between the $2p_{1/2}$ and $2p_{3/2}$ lines also becomes much deeper after the exfoliation. The “shoulder narrowing” is particularly large at the high binding energy side. The right-hand plot shows the corresponding S LMM Auger peak that also shows a similar trend, with a narrowing of the Auger line at lower kinetic energies. The broadening in the as-received measurement likely corresponds to the presence of Mo_xO_y, MoS_3, and/or sulfites.[19,77]

The plot in the center shows fits of the S 2p region for the exfoliated crystal surface. The region was fitted with a linear background and several Voigt profiles with area ratios fixed according to the multiplicity (2j+1), using the peak-fitting program Fityk.[82] Three spin-orbit doublets of Voigt profiles representing three different chemical species were used. The shape of the Voigt profiles was kept constant while the width was allowed to vary between the different pairs. The raw data is represented with black open circles, while the sum model is shown as a red line and the components are shown as green, blue, and pink lines. The indicated the presence of at least three prevalent chemical species of S 2p are present.

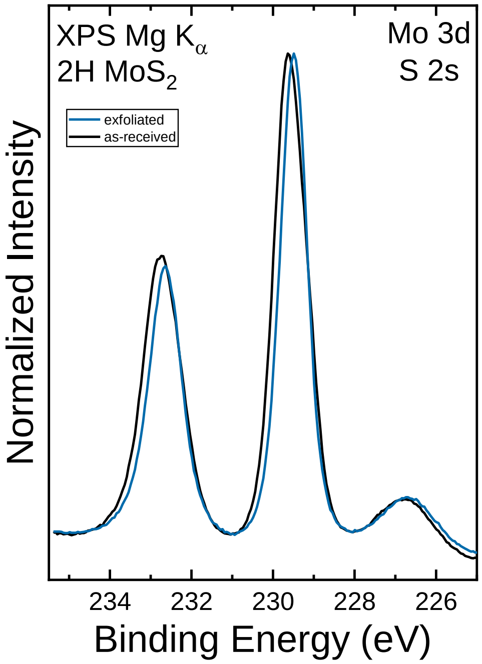

Figure 3.6: Mo 3d and S 2s XPS Mg K_α region for the as-received and exfoliated measurement round for the 2H phase MoS_2 single crystal. The intensity shown here is normalized to the peak maximum.

Figure 3.6 shows the Mo 3d and S 2s region of the as-received (black line) and exfoliated (blue line) 2H phase MoS_2, with a normalized intensity such that the intensity at 228 eV is the minimum and the peak maximum of the Mo $3d_{5/2}$ is the maximum. The S 2s peak is positioned between 228 to 225 eV while the other two peaks at higher binding energies correspond to the Mo 3d peaks. By comparing the normalized Mo 3d peaks, it can be noted that the the peak maxima for both Mo 3d peaks shift to lower binding energies, however the peak width becomes narrower after the exfoliation.

3.2.2 Confirming the 2H phase in MoS_2 single crystal

Since the MoS_2 single crystal has several typical structures, namely 2H, 1T, and 3R, it is possible to verify the phase of the crystal using XPS and LEED.[4,5]

As seen in Figure 3.6 of the previous section, the $Mo3d_{3/2}$ peak of the exfoliated sample is positioned at 232.65 ± 0.05 eV and Mo 3d $3d_{5/2}$ is positioned at 229.50 ± 0.05 eV. These values correspond to a Mo^{4+} oxidation state and the 2H-phase, as seen in previous XPS studies of the material where the energies of the Mo 3d peak are typically 1 eV lower (binding energy) compared to the 1T or 3R phases of MoS_2.[14,75,80,83] Similarly, the position of the S $2p_{1/2}$ at 163.50 ± 0.05 eV and S $2p_{3/2}$ at 162.30 ± 0.05 eV also indicate the presence of the 2H phase, with the 1T phase that would typically be positioned at lower binding energies by 1 eV.[14]

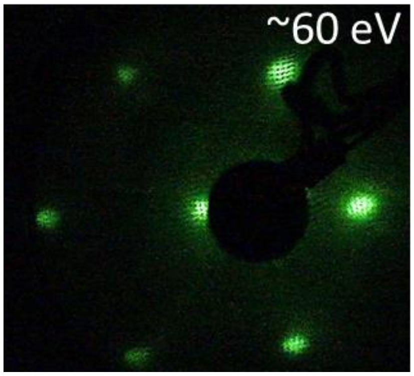

Figure 3.7: LEED pattern of the exfoliated 2H phase MoS_2 single crystal surface with a bias voltage of approximately 60 eV.

The LEED pattern seen in Figure 3.7 also verifies the 2H phase of the MoS_2 single crystal and is found in previous studies of the material.[84–87] The image shows a well-defined hexagonal or "honeycomb" pattern, confirming the hexagonal structure of the 2H MoS_2 crystal in reciprocal space. The quality of the image also affirms the highly ordered nature of the synthetic crystal surface, despite the large amount of carbon present on the surface of the crystal (this is due to the fact that only the well-ordered surface atoms scatter coherently and thus contribute to the LEED pattern). The differences in the spot sizes of the pattern can be a result from a slightly tilted sample position.

3.3 Conclusion

To summarize this chapter, XPS was utilized to investigate the surface chemical structure of an as-received 2H phase MoS_2 single crystal that was then mechanically exfoliated using adhesive tape in an environmentally controller glovebox and without any exposure to air. Exfoliating the MoS_2 surface removed some of the carbon and oxygen signal, while increasing the signals of Mo- and S-related peaks. After accounting for differences in photoionization cross-sections, analyzer transmission function, and inelastic mean free paths, the surface stoichiometry was found to be C : O : Mo : S = 29% : 5% : 20% : 45% for the as-received surface, which modified to C : O : Mo : S = 25% : 3% : 22% : 50% after mechanical exfoliation. This indicates the prevalence of Mo and, especially, S in the MoS_2 crystal surface structure, as expected, but also the presence of a significant amount carbon impurities.

Further analysis of the chemical species present before and after the exfoliation in the C 1s and O 1s regions showed that the peaks remained at similar binding energies but their shapes had changed. After the exfoliation, the C 1s peak appeared broader close to the peak maximum, with a chemical environment of carbon, hydrocarbons, carbon bound to sulfur, and/or carbon bound to molybdenum. The difference in the normalized O 1s peak showed at least one additional component found in the as-received surface that can correspond to sulfates, $Mo(O_xS_y)_2$, and/or hydroxides. Evaluation of S 2p and Mo 3d regions shows other indications of how the exfoliation affected the surface composition and other properties. A S/Mo ratio of 2.00 ± 0.05 was derived for the exfoliated crystal surface, indicating the possibility of molybdenum vacancies. Finally, XPS and LEED were also used to verify the 2H phase of the MoS_2 crystal structure at the surface of the exfoliated sample.

CHAPTER 4: ELECTRONIC STRUCTURE OF A 2H MOS_2 SINGLE CRYSTAL

4.1 Experimental Details

To study the electronic properties of 2H phase MoS_2, the exfoliated single crystal (15 x 7 x 1 mm^3 in size) was measured with UPS using monochromated He I and II excitation (with excitation energies of 21.2 and 41.8 eV, respectively) from a Gammadata VUV 5000 source and a Scienta R4000 electron analyzer. This technique was combined with IPES, which was measured using a STAIB NEK-150-1 low-energy electron gun, a photon detector with a Semrock Hg01-254-25 mercury line filter, and a Hamamatsu R6834 photomultiplier.[43] An Ag foil was cleaned using Ar^+ ion sputtering and measured to determine the Fermi edge. The mechanical exfoliation of the single crystal was performed using adhesive tape as described in Chapter 3.[5,8,11–17] The exfoliation was performed multiple times to remove several layers from the surface. Although each layer peeled off easily, these layers were uneven and resulted in a surface that was not completely flat on a macroscopic scale, creating challenges with angular resolved photoelectron spectroscopy (ARPES) measurements.[59,60]

At the Advanced Light Source (ALS), Lawrence Berkeley National Laboratory, an as-received 2H phase MoS_2 single crystal was measured at Beamline 8.0.1 using RIXS. A two-dimensional RIXS map is shown in this chapter, which combines both XES and XAS in a resonant one-step scattering process that gives information about the local band structure of solids (a more detailed discussion can be found in Section 2.2.2). This technique gives information about the local electronic valence environment of the S atoms in the near-surface bulk region. The excitation and emission energy scales were calibrated using reference measurements and literature values for BN and $CaSO_4$.

In addition, density functional theory calculations were performed using the WIEN2k program package to aid in the analysis of the density of states and band structure (described in further detail in Section 2.3.3).

4.2 Results and Discussion

4.2.1 Valence band structure comparison

To gain an overview of the measured occupied electronic structure between different spectroscopic techniques employed in this study, Figure 4.1 shows how the valence band structure of the 2H phase MoS_2 single crystal varies with the following lab- and synchrotron-based techniques: XPS Mg K_α (blue line), UPS He I (black line), non-resonant XES (green line), and the calculated total density of states (red line). The non-resonant x-ray emission spectrum shown in this plot was integrated between excitation energies of 170.09 and 174.89 eV (as seen in the RIXS map in Figure 4.3, to be discussed below), where the x-ray emission spectrum does not noticeably change as a function of excitation energy. The energy scale in Fig. 4.1 is relative to the derived valence band maximum (VBM), and the intensity is normalized to the maximal intensity for each measurement.

Most of the bands contributing to the valence band structure correspond to S 3p and Mo 4d molecular orbitals. Strong variations in the relative intensity of spectral features are present, although most of the features are positioned at similar energies between the different techniques. In the XPS Mg K_α spectrum, additional spectral lines may be present from contributions of satellites since a non-monochromated x-ray source way used for this measurement. The broadest features are present in the XPS Mg K_α while the narrowest are present in the theorical DOS calculation, which does not account for

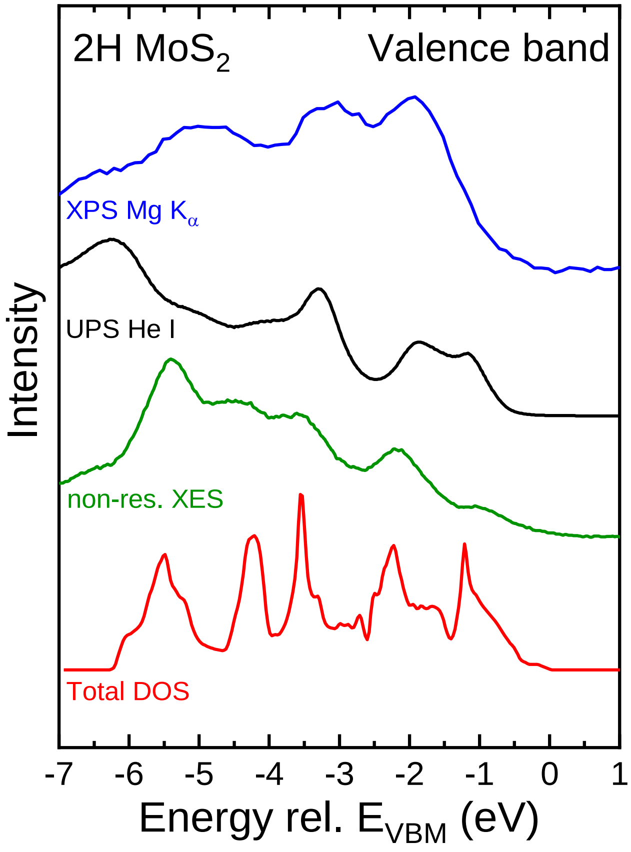

Figure 4.1: Valence band structure comparison of the 2H MoS$_2$ single crystal measured with various spectral techniques, XPS Mg K$_\alpha$ (blue), UPS He I (black), non-resonant XES (green) integrated from 170.09 to 174.89 eV excitation energy, and the calculated total density of states (red). The energy is given relative to the derived valence band maximum (VBM).

experimental and lifetime broadening.[88] The spectral features, particularly between non-resonant XES and UPS, coincide well as these techniques have the same final state (valence hole for UPS and XES, while a core hole for XPS).[27,30] Since XES probes the local environment at the S 2p core hole, its initial state is different for XPS and UPS where the initial state is the ground state. While the final states effects are the same between the techniques, transition dipole moment matrix elements differ as given by Fermi's Golden Rule, and as outlined in Section 2.2.2. The differences in the spectral shape and relative intensities may also be due to different amount of surface contaminations and the sensitivity of the technique to them.

4.2.2 Effects of mechanical exfoliation on the valence band structure

To complement the discussion from Chapter 3 on the effects of exfoliation on the chemical structure of the MoS_2 crystal, it is also possible to observe how the electronic structure changes, as will be done in this section. Figure 4.2 shows UPS spectra taken with monochromated He I excitation energy of the secondary electron cut-off on the left-hand side, and valence band structure in the center and right-hand plots. The as-received 2H phase MoS_2 single crystal is indicated by the black line while the exfoliated crystal surface is indicated by the blue line. The intensity of the spectra in these plots have all been normalized to the peak maximum height to better compare the differences in their spectral shape and energy position. In the valence band structure, the spectral shape and background differs substantially between the as-received and exfoliated surfaces, making it challenging to compare their features. Here, the intensity of the center plot is normalized so that the background is set as the minimum and the spectral shape at higher energies (approximately 8.5 eV) is set as the 1. The plot to the right focuses on the valence band region closer to the Fermi energy and was normalized so that the intensity of the peak at 2.5 eV is set to the maximum. The abscissa reported in this section are energies relative to the Fermi energy determined using a reference Ag foil.

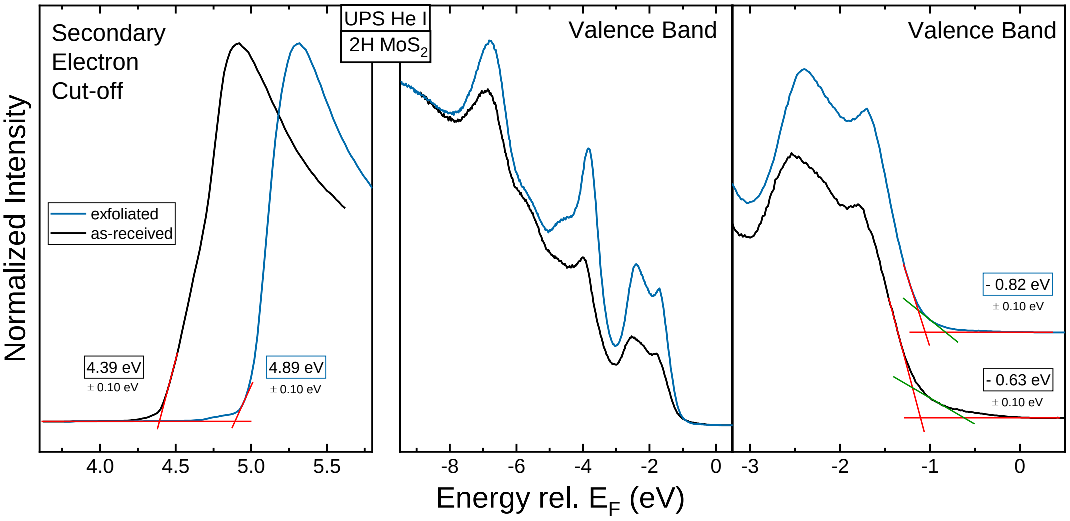

Figure 4.2: Secondary electron cut-off and valence band structure measured with He I UPS are shown for the as-received (black) and exfoliated (blue) 2H phase MoS_2 single crystal. The secondary electron cut-offs and the derived work functions are shown in the left-most plot, the valence band is shown in the center and right-hand plots, with the derived band edges. The intensity of all regions is normalized to the peak maximum height.

The secondary electron cut-off can be used to obtain the work function at the surface of the material using linear extrapolation. Since the work function is sensitive to any differences in surface adsorbates, impurities, or surface defects, it is a surface property that gives information about a specific chemical environment. For the as-received sample, the work function was derived at 4.39 ± 0.10 eV and shifts to higher energies at 4.89 ± 0.10 eV after the exfoliation was performed. The value of the work function for both of the measurements is higher than most of the previously reported values for a 2H phase MoS_2 single crystal but is closer to the work function derived for MoS_2/MoO_2 films, with a 4.7 eV work function using UPS.[80] A work function of 4.92 eV was previous found using UPS for the surface of a MoS_2 film that was modified with an C_{60} overlayer.[89] Given the high carbon intensity found using XPS in Section 3.2, the value of the work function may be higher as a result. Other work functions of 2H phase MoS_2 were derived at 4.13 eV using UPS and 4.59 eV using Kelvin probe force microscopy (KPFM).[75,90] These studies also showed that different substrates, like SiO_2, used with MoS_2 flakes affect the work function of the material.[75,90] In other studies using scanning tunneling microscopy, the increase of the work function has been attributed to the formation of sulfur vacancies in 2H MoS_2 single crystals.[91] Not only does the energy change, but the shape of the onset of the secondary electron cut-off is different before and after the exfoliation. Care was taken to ensure that the UPS beam was not over the sample plate or the grounding clip for all measurements, however, the onset of the secondary electron cut-off is not completely vertical. The shape of the onset becomes slightly steeper after the exfoliation which may be due from the removal of adsorbates present of the surface or slight variations in the measurement position of the single crystal.

The valence band shown in the center and right-hand side of Figure 4.2 also demonstrates distinct differences in the valence band structure before and after the exfoliation. The shape of the features found at 7, 4, and 2 eV become more defined following the exfoliation. From partial density of states calculations conducted in this work and found in literature, the spectral features of the valence band around 6-7 eV is dominated by contribution primarily from S p_x, S p_y, and S p_z orbitals, while the feature at 4 eV is dominated by Mo $d_{x^2-y^2}$ and Mo d_{xy} orbitals.[10]

The plot on the right-hand side of Figure 4.2 shows the valence band at closer energies to the Fermi energy. The foot and the leading band edge changes after the exfoliation, suggesting that the change in line shape can represent the removal of adsorbates on the surface of the crystal. Based on partial density of state calculations in with work and other studies, bands corresponding to S 3p orbitals, primarily p_z and p_y derived states, and Mo 4d orbitals, primarily d_z^2 and d_{xy} derived states, are the main molybdenum and sulfur related contributions to the valence band structure close to the Fermi energy.[2,48,87] As in other studies of the experimentally measured electronic structure, the leading valence band edges can be derived using linear extrapolation. Linear extrapolation is a suitable method of deriving the uppermost electronic states of the valence band since valence band spectra shown here are integrated over k-space, have non-symmetric broadening as a result of limited angular resolution of the electron analyzer, with inelastic scattering processes and incomplete screening that may lead to shifts of bands to higher binding energies.[23–25]

The leading band edge of the as-received MoS_2 crystal was found at 0.63 ± 0.10 eV (using green lines), which shifted away from the Fermi energy to 0.82 ± 0.10 eV after the exfoliation. The values derived here are lower compared to other studies of MoS_2 films and single crystals using UPS, which ranged from 1.5 to 0.9 eV.[75,80] A similar foot is found in the measured valence band in these studies, but the linear extrapolation used here is taken much closer to the foot and the references studies are one films in a MoS_2/MoO_2 environment.[80] The foot may be a result of elastic scattering and final state effects.

4.2.3 Momentum-resolved measurements of 2H MoS_2

Techniques like angular resolved photoelectron spectroscopy can directly probe not only energy-resolved but also momentum-resolved (or k-resolved) electronic structure. Due to the translational symmetry of the crystal in the x and y directions, the in-plane momentum components of k_x and k_y are conserved within the photoemission process.[92] The emission angle detected by the electron analyzer corresponds to the momentum of the ejected photoelectrons (further information about ARPES can be found in reference [93]). ARPES has been utilized in many studies looking at the electronic structure of MoS_2. In bulk 2H phase MoS_2 investigations, the main features of the MoS_2 band structure originate from Mo 4d states and are in good agreement with results from theoretical calculations.[10,58,94,95] Studies show that the S p orbitals shield the Mo $4d_z^2$ orbitals, resulting in a decrease of the intensity around the Γ point in the ARPES maps.[58,87] Spin-split bands around the K point are also reported due to spin-orbit interaction and broken inversion symmetry, the splitting may be large enough that it induces a transition from an indirect to direct bandgap.[10,58,84,94,96] K_z dispersion in bulk 2H phase MoS_2 is strong near the Γ point using photon-energy dependent ARPES with no measured k_z dispersion around the K point.[94] With increasing interlayer distance in MoX_2 compounds, the Mo $4d_z^2$ band is shifted towards higher binding energy and dispersion decreases.[87]

There are many challenges presented with measuring ARPES as this techniques is sensitive to any surface contaminations, and the sample rotation can modify the photoemission matrix elements, polarization geometry, or beam position on the sample.[38,39] Most studies looking at this materials use a monolayer of MoS_2, which is difficult to grow on a wafer scale.[94] Monolayer MoS_2 with a substrate has been observed to distort the band structure and measurements of optical and electronic properties of the material, and in most cases such substrates (e.g., Si/SiO_2) lead to a measured MoS_2 that is n-doped.[97–99]

Further investigation into the electronic structure can be done by utilizing RIXS. The absorption and emission processes are a one-step resonance inelastic process (further discussion in Section 2.2.3) with a crystal momentum that is conserved within the transition. In the soft x-ray region, the momentum transferred from the incident photon to the sample is negligible relative to the crystal momentum, and the momentum of the electron in the conduction band is equal to the momentum of the electron in the valence band (i.e., the excitonic transition occurs along the same k-point).[32,35] The emission spectrum is dependent on the excitation energy as different k-points of the Brillouin zone are probed. At high-symmetry points of the Brillouin zone, the information of the occupied and unoccupied states can be more easily separated, especially at the VBM and the CBM. For this material, since the reported value of the high-symmetry point for the VBM varies between the Γ and K point depending sample thickness of the MoS_2,[9] this may be challenging but important to identify the high symmetry points that the VBM and CBM is positioned at.

RIXS maps have been successfully used to study the band structure of solid material systems like C_{60}, water, and various chalcogenides.[100–104] The S $L_{2,3}$ emission allows s and d character to be probed and for the overlap of the Mo 4d with the S 2p core hole wave functions to be observed. Compared to angular resolved PES, because RIXS is based entirely on photons, it probes the true bulk properties and is not influenced by surface contaminations, while techniques like ARPES are sensitive. RIXS is also insensitive to sample charging and external electric or magnetic fields, but it is element specific and offers angular momentum sensitivity via resonant excitation.[105,106] This also allows for the sample preparation to be performed outside of an inert environment and without the need for additional surface treatments or exfoliation.

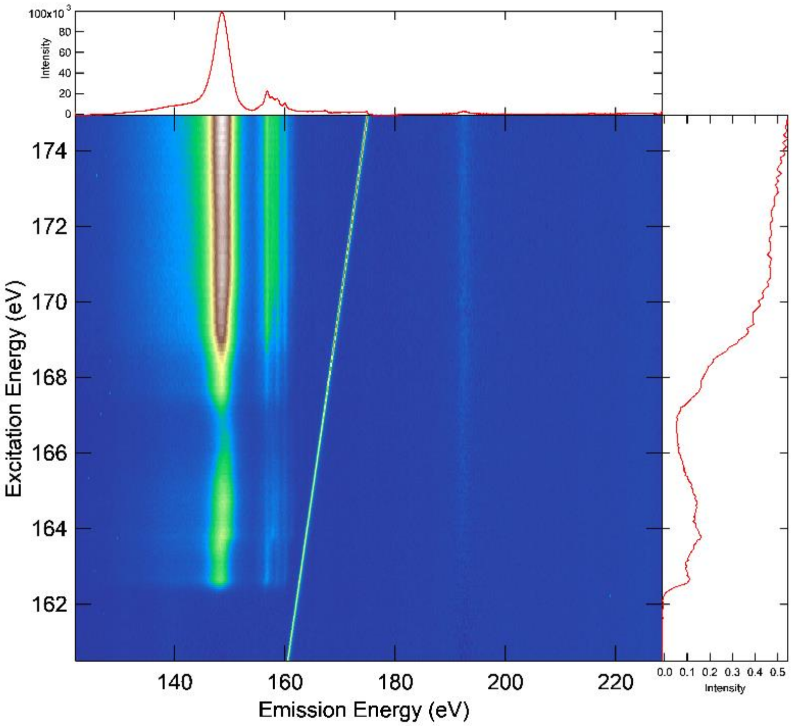

Figure 4.3: Two-dimensional RIXS map of an as-received 2H phase MoS_2 crystal. The upper panel shows the XES spectrum integrated across all excitation energies present in the map, while the panel on the right shows the XAS spectrum integrated across all emission energies.

The two-dimensional color-coded S $L_{2,3}$ RIXS map of an as-received 2H phase MoS_2 single crystal is shown in Figure 4.3 with the emission energy as the abscissa and excitation energy as the ordinate. The lowest intensity is shown by the blue color and the highest intensity of the map is shown by the white. The diagonal line going across the map refers to the Rayleigh line that is a result of elastic scattering and represents the energy of the exciting photons (with equal excitation and emission energies).[101] Three separate maps were measured and combined together in Figure 4.3, with excitation energies of 160.56 - 161.56 eV and 167.72 - 175 eV collected with a 0.1 eV step size, while 161.56 - 167.72 eV was collected with a 0.05 eV step size. The 161.56 - 167.72 eV range represents the resonant portion of the map as the features change as a function of excitation energy. Above the map, the XES spectrum integrated over all excitation energies is shown, while the plot to the right shows the XAS spectrum integrated over all emission energies of the map. The feature at around 148 eV emission energy refers to transitions from the S 3s-derived band while the feature between 155 to 161 eV emission energy are the transitions from the upper valence band.[100,101,107] The feature with weaker intensity at 192 eV emission energy corresponds to a transition from Mo 4s into the S 2p core hole in the second harmonic of the undulator beamline (and the second order of the beamline grating). Each transition forms a doublet as a result of the spin-orbit splitting of the S 2p core holes, with a distinct separation of 1.2 eV.[101]

From the RIXS map, contributions from S L_2 and L_3 edge can be separated, as shown in Figure 4.4. The spectrum at the top refers to the S L_2 edge integrated over 163.71 to 164.89 eV excitation energies from the RIXS map, while the spectrum at the bottom shows the S L_3 edge integrated over 162.48 to 163.66 eV. The intensity of both spectra was normalized with the minimum intensity set to zero and the maximum height of the peak set to one. The scatter points represent the data points of the measured spectrum, while the red line represents the model, the green and blue lines represent the two components used to fit the spectrum. The components used to fit both spectra are

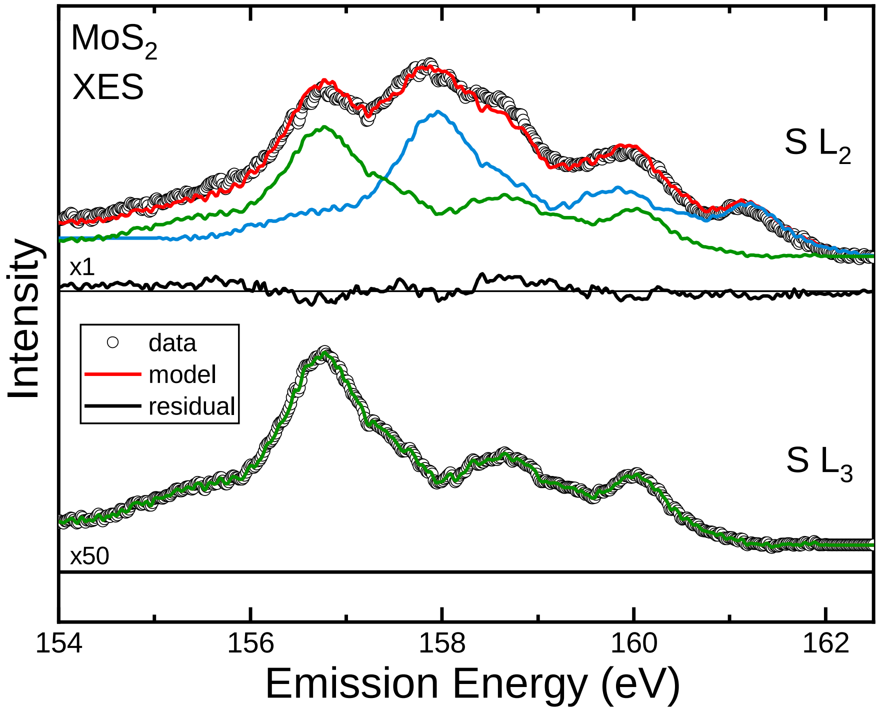

Figure 4.4: Separated S L_3 and S L_2 regions of XES data of the 2H phase MoS_2 single crystal. The bottom spectrum is the S L_3 emission (integrated over 162.48 to 163.66 eV excitation energies), while the top spectrum is the combined S $L_{2,3}$ emission, integrated over 163.71 to 164.89 eV. It can be described by two "copies" of the S L_3 emission spectrum, separated by the spin-orbit splitting of 1.2 eV, as shown in the upper panel.

the extracted S L_3 spectrum, which is why the green component matches the sum (red) line and the residual is flat for the bottom spectrum. For the S L_2 spectrum, the green component in this fit is the exact same as the green component for S L_3 while the additional blue component is then shifted over by 1.18 eV. The fit for the S L_2 edge is not perfect, as indicated by the residual between the model and the measured data points. This, at least in part, is due to the noise in both spectra depicted in this figure. In addition to showing the integrated XES regions, it is also possible to show the individuals scans from the RIXS map as a function of excitation energies.

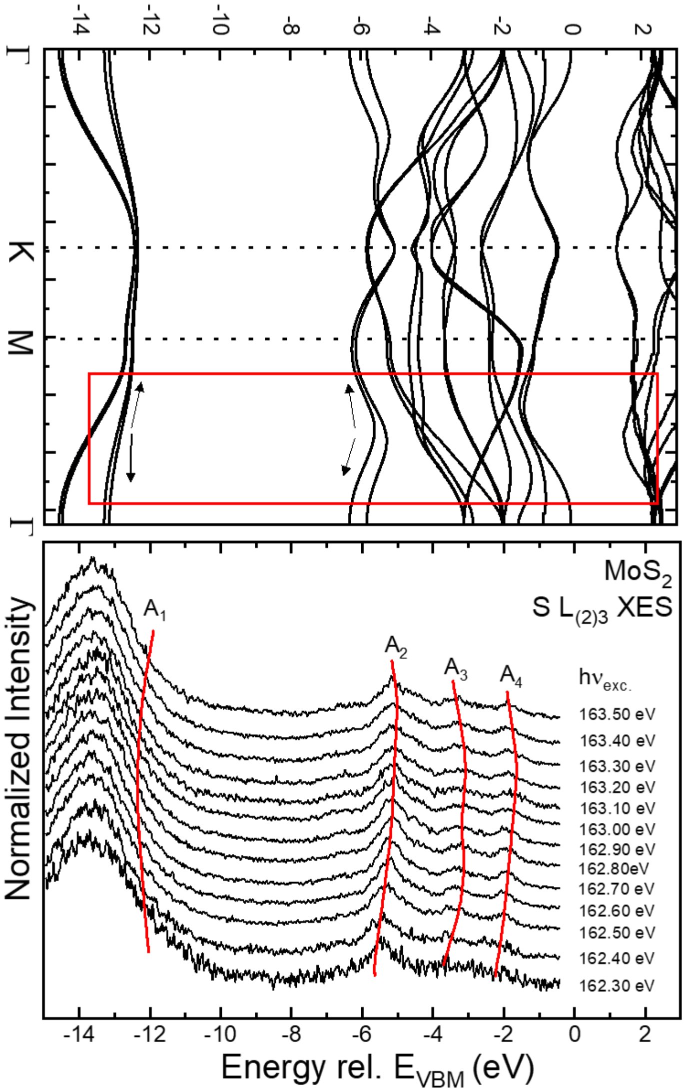

Figure 4.5: S L$_{(2)3}$ emission spectra extracted from the RIXS map with the excitation energy shown to the right. The intensity for all spectra is normalized to the peak maximum height. The plot above the XES spectra is the calculated band structure of the MoS$_2$ using DFT calculations. Observed shifts in the spectra are indicated by the red likes and labels with the corresponding proposed bands highlighted by the red box in the band structure. The energy scale is relative to the valence band maximum.

Figure 4.5 shows the extracted XES spectra at a specific excitation energy, each spectrum showed is an average of two scans to improve the signal-to-noise ratio of the data. Intensity for all spectra has been normalized to the peak maximum height. Above the extracted XES spectra, a band structure of the MoS_2 calculated using first principle DFT calculations is also shown. The energy scale for the XES spectra is relative to the overall VBM, found by extracting the highest emission energy (161.94 eV) from the RIXS map in Figure 4.3. This was done to have a more direct comparison to the calculated band structure that has an energy scale that is also relative to the VBM. The shifts in the spectral features as a function of excitation energies are indicated by the red lines and labels with four main features that are observed. The red box in the band structure corresponds to the proposed bands that the measured XES spectra could be attributed to. The dispersive features appear to take place between the Γ and M high-symmetry points. Other dispersion features may not be present due to the localized nature of the Mo 4d wavefunctions and small overlap with the S p wavefunction. It may also be difficult to track the band dispersion as many of the bands possess relatively flat dispersion along the high-symmetry points of the band structure.

4.2.4 Bandgap of 2H MoS_2

A wide range of calculated and experimentally derived bandgaps of MoS_2 are present in literature. Table 4.1 shows the values of indirect and direct bandgaps from specific studies with theoretical calculations on the top portion of the table and experimentally derived values on the bottom portion. Provided sample information, year that the study was published and the corresponding references are also included. As seen

	Indirect E_g (eV)	*Direct E_g (eV)*	*Material*	
LDA	1.29	1.78	2H MoS_2[58]	2001
		1.78	MoS_2[108]	2009
LDA+lo	0.75	1.89	2H MoS_2[109]	2012
PBE-GGA	0.8		MoS_2[110]	2010
	0.86	1.8	2H MoS_2[111]	2007
	0.9	1.57	MoS_2[48]	2014
	1.2		2H MoS_2[112]	2011
	1.29		2H MoS_2[113]	2012
	1.52	1.72	MoS_2[114]	2012
PBE0-GGA	2.2		2H MoS_2[112]	2011
PBE-GGA DZP basis	1.06	1.70	MoS_2[115]	2010
GGA+lo	1.05	1.55	2H MoS_2[109]	2012
APW+lo	0.65	1.79	2H MoS_2[116]	2012
GGA	1.26	1.85	MoS_2[117]	2019
FLAPW	0.9	1.7	2H MoS_2[95]	2012
LDOS	0.77		2H MoS_2[118]	1995
HSE	1.60		MoS_2[119]	2011
APW	1.2		2H MoS_2[120]	1973
simplified linear combination of MT orbitals	1.1	2.7	MoS_2[121]	1973
Crystal field	1.35		MoS_2[122]	1971
PL	1.29	1.90	MoS_2 on SiO_2 substrate[8]	2010
PL	~1	~2	MoS_2 on SiO_2 substrate[9]	2010
ARPES and IPES	1.4		Na doped MoS_2(0001)[123]	2014
ARPES and LAWP	1.29	1.78	MoS_2(001) flakes[87]	2012
ARPES and KRIPES		2.11	MoS_2 monolayer on sapphire[99]	2018
trARPES and STS		2.15 (STS)	MoS_2 monolayer on HOPG[84]	2021
ARPES and STM	1.14	1.82	2H MoS_2 single crystal	2013

Table 4.1: Calculated and experimentally derived indirect and direct bandgap values for 2H phase MoS_2 found in literature.

in Table 4.1, the values range from 0.65 eV to 1.60 eV for indirect bandgap values and from 1.55 to 2.7 eV for direct bandgaps. Although not all studies specify a 2H phase MoS_2, the 2H is the thermodynamically stable phase compared to the other phases seen with MoS_2 that need to be specifically altered through doping.[3] There are many reasons for the wide array of derived bandgaps, for the experimentally derived values the differences are a result of sample preparation (monolayer with a substrate versus bulk crystal) and type of techniques (i.e., optical versus electronic measurements), incorrect reference energies (e.g., using the vacuum level as the reference energy), and the complex characteristics of MoS_2 and other transition metal dichalcogenides. Complex characteristics of MoS_2 are present through the covalently bonded S-Mo-S sheets that are weakly bonded by van der Waals forces.[5] The three main phases of MoS_2 single crystal, 2H, 1T, and 3R have reported different electronic structures, with the 2H and the 3R phase that behave more like a semiconductor while the 1T is metallic in nature.[3]

One of the most discussed aspects about MoS_2 is its thickness-dependent bandgap that seems to transition from an indirect bandgap in its bulk form to direct bandgap when a monolayer of the MoS_2 is present with a substrate. Studies using photoluminescence (PL) saw an evolution of optical properties with specific layers of MoS_2 on oxide-covered Si substrates with high photoluminescence detected from a sample that had only one monolayer of MoS_2 on the substrate.[8] A similar study of ultra-thin MoS_2 on a Si/SiO_2 substrate was performed with photoluminescence also found strong photoluminescence with a monolayer of MoS_2.[9] This spike in the photoluminescence has been attributed to the evolution of the MoS_2 indirect bandgap in its bulk form to a direct bandgap when only a monolayer of the MoS_2 is present. When studied with Raman spectroscopy, the MoS_2 (also on a Si/SiO_2 substrate) saw a Raman modes E^1_{2g} and A^1_g exhibit sensitivity to thickness.[124]

One of the most widely accepted causes of this bandgap evolution is due to the weak van der Waals interlayer interactions that affect the intralayer bonding of the few-layer molybdenum disulfide.[113] Direct excitonic transition energy at K point stays relatively the same while the bands around the Γ point change ("compresses" and becomes less disperse) and the indirect transition energy becomes too high. The states near the Γ point in the valence band and K point in the conduction band originate from linear combination of delocalized Mo d_z^2 orbital and antibonding S p_z orbitals. They have strong interlayer coupling and their energies depend on layer thickness while states near K point are mostly comprised of orbitals localized in the xy plane and not affected by the layer-layer interaction.[9,87,95,111,113] With a monolayer system, the interlayer coupling is not present and therefore creates the direct bandgap MoS_2.[8] Others identify the presence of Coulombic interlayer interactions in MoS_2 have a more prominent effect on the electronic structure of MoS_2 than weak van der Waals forces.[124] Finally, as discussed in Section 4.2.3, the effects of the spin band splitting around the K point as a result of spin-orbit interaction and broken inversion symmetry has been argued to be drastic enough to cause a transition from an indirect to a direct bandgap of the MoS_2.

For monolayer MoS_2, a study had reported on the role of point defects on the photoluminescence intensity due to vacancy generation.[125] The study poses that free charge carries and localized electrons interactions become stronger due to reduced dimensions, which lead to light emission at energies lower than the band-to band optical transition energy if radiatively recombined. Substrates can also play a role for few layer

MoS_2, studies looking at the effects of substrates used with monolayer MoS_2 proposed that it is the relaxation of the in-plane lattice that causes the compression of the dispersion at the Γ point that was discussed earlier.[11,97] The influence of the substrate decreases strongly with increasing layer number.[98]

Here, the surface electronic bandgap can be found by using UPS to derive the valence band and IPES to experimentally measure the conduction band. By combining

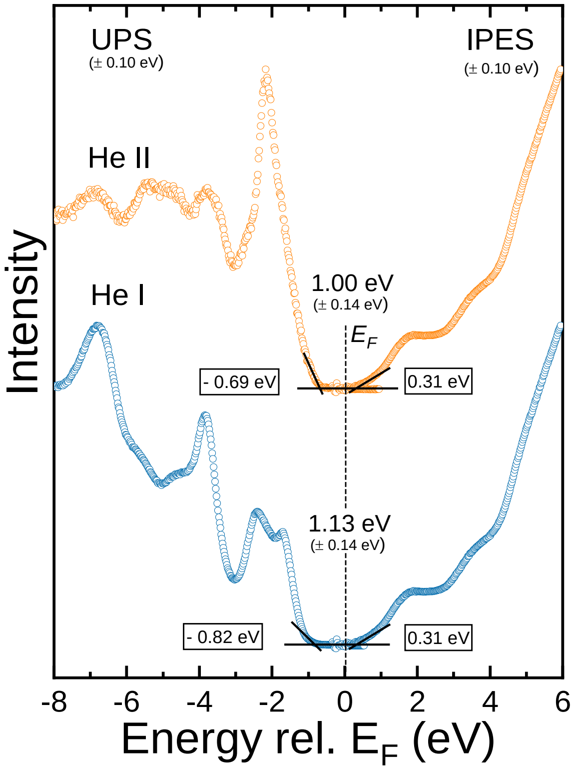

Figure 4.6: UPS (left) and IPES (right) spectra with respect to the Fermi energy (E_F) of the cleaved 2H phase MoS_2 crystal with He I UPS on the bottom left and He I on the top left side (orange) of the plot.

the two measurements together, with a common energy axis that is relative to the Fermi energy, the VBM and CBM can be uncovered using linear extrapolation of the leading band edges, as is shown in Figure 4.6 of the exfoliated 2H phase MoS_2 single crystal. The CBM is found to be 0.31 ± 0.10 eV while the VBM varies between He I and He II excitation energies. For He I UPS, the VBM is found at 0.82 ± 0.10 eV and shifts closer to the Fermi edge at 0.69 ± 0.10 eV with He II excitation. The same IPES spectrum is used in both instances. By combining the value of the VBM and CBM, the surface bandgap is derived at 1.13 ± 0.14 eV using the He I spectrum and 1.00 ± 0.14 eV using the He II spectrum. The shape of the valence band measured with He I and He II have distinctly different shapes, most prominently at around 2 eV. This feature is attributed to contributions from Mo 4d orbitals, which has a far more pronounced photoionization cross section at 40 eV ionization energy (He II) rather than He I, compared to the S 3p bands that contribute to the valence orbital shape.[10,95]

From the RIXS map discussed earlier, it is possible to derive several bandgap values at various k-points in the Brillouin zone, as done with beryllium chalcogenides in past studies utilizing the RIXS process.[104] As previously stated, the highest emission energy overall was found at 161.94 eV and refers to the VBM. The excitation energy of the spectrum with the highest emission energy was also found at 163.81 eV and corresponds to the conduction band at the same point in k-space as the VBM. From this, a direct bandgap at the VBM (i.e., a vertical transition from the valence band to the conduction band at the same k-point) is derived at 1.87 eV. The onset of absorption as a function of excitation energy corresponds to the overall CBM, which was found at 162.29 eV. The derived CBM value here is slightly different from the CBM found specifically at

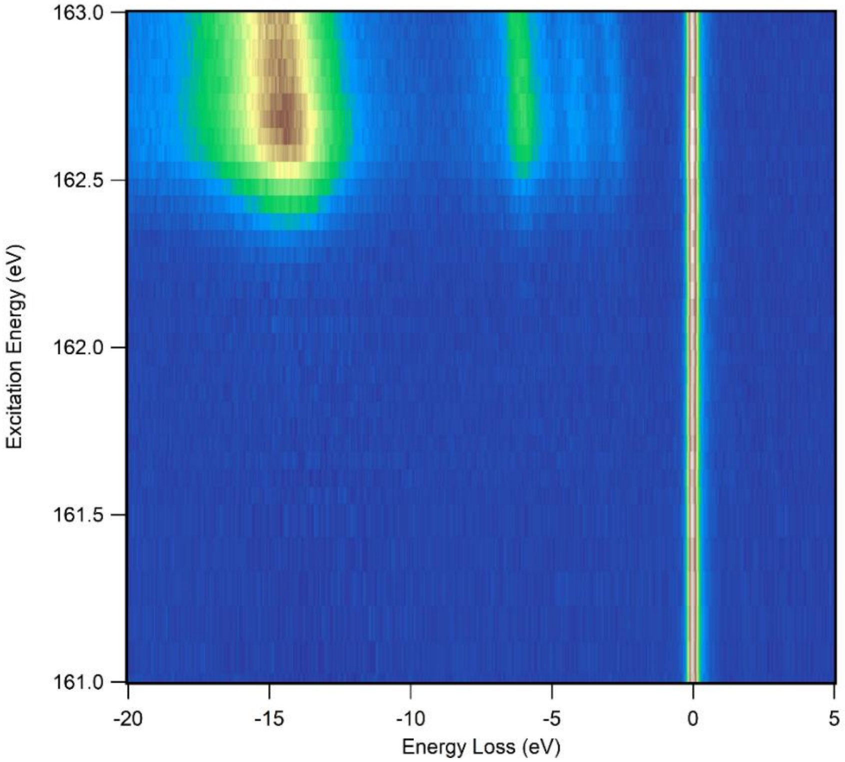

Figure 4.7: Near-edge region of the S $L_{2,3}$ RIXS map of the 2H phase MoS_2 single crystal (Figure 4.3), plotted as a function of energy loss with respect to the Rayleigh line (which is consequently is depicted as a straight vertical line).

the lowest excitation energy for observed emission, which was found at 162.17 eV. A direct bandgap at CBM of 1.66 eV is found using the highest emission energy at the lowest excitation energy. To check for possible Raman shifts, the emission energies of the Rayleigh line in the RIXS map from Figure 4.3 can be shifted so that the Rayleigh line is a straight line instead of a diagonal one and set as the 0 eV emission energy, as shown in Figure 4.7. This is another way to see if there are any Raman shifts present in the map, which would be parallel to the elastic Rayleigh line. However, the zoomed in region gives little indication of a Raman loss feature, which would have been present at excitation energies below 162.5 eV.

Table 4.2 provides a summary of the derived bandgap values for the 2H phase MoS_2 single crystal using He I and He II UPS, IPES, and RIXS. The variations in bandgap values derived from UPS He I and He II excitation energies have already been discussed and can be attributed to contributions from different bands that are probed by these two excitation energies. In addition, these two bandgap values are within the confidence interval of ± 0.14 eV. For RIXS-derived bandgaps, the values of the direct bandgap at VBM is different from the direct bandgap derived at the CBM. Assuming that the momentum is conserved within the RIXS process, and the bandgap of a bulk MoS_2 single crystal is truly an indirect bandgap, then the different values found though the RIXS data is acceptable since the direct transition at the CBM and VBM occur at different k-points.

Bandgap value	Techniques used to derive value
1.13 ± 0.14 eV	He I UPS and IPES
1.00 ± 0.14 eV	He II UPS and IPES
1.87 eV	Direct bandgap at the VBM
1.66 eV	Direct bandgap at CBM

Table 4.2: Summary of the experimentally derived bandgaps value of the 2H MoS_2 single crystal using UPS, IPES, and RIXS.

4.3 Conclusion

To summarize the findings of this chapter, a comparison of the various spectroscopic technique was done to see how the signature of the valence band differs between the various spectroscopic techniques employed in this study. Due to differences in the final and initial states, transmission matrix elements, and sensitivity of surface contaminants, the spectral features are different. Afterward, the effects of the mechanical exfoliation on the electronic structure of the 2H phase MoS_2 single crystal surface was investigated. A work function of 4.39 ± 0.10 eV was derived for the as-received crystal, which shifted to higher energies of 4.89 ± 0.10 eV after the exfoliation was performed. The spectral features of the valence band region change drastically after the exfoliation, and the linearly extrapolated VBM was found at 0.63 ± 0.10 eV and shifted to 0.82 ± 0.10 eV after the exfoliation. RIXS was performed to find the bulk electronic properties and the momentum-resolved characteristics of the MoS_2 crystal. The extracted XES spectra contained spectral features that evolved as a function of excitation energy and corresponded to specific states in the band structure. In this study, the derived surface bandgap was found at 1.13 eV using the He I UPS spectrum and 1.00 eV using the He II UPS spectrum, when combined with the IPES measurement. From RIXS, a direct bandgap at the CBM was found at 1.66 eV while a direct bandgap at the VBM was found at 1.87 eV. In addition, XES spectra were extracted from the RIXS map and used to identify possible band dispersion that correspond to transitions at various k-points in the Brillouin zone of the crystal.

CHAPTER 5: CONCLUDING REMARKS

MoS_2 and other transition metal dichalcogenides have an extensive list of applications, particularly in energy conversion and storage devices. For example, they can be incorporated as flexible substrates or thin contact layers for thin film solar cells, as well as batteries and electrocatalyst for the hydrogen evolution reactions. However, a further understanding of this material system is essential to optimize the performance of such devices and components, particularly by gaining insights into its electronic structure. For MoS_2, the bandgap has been previously reported to transition from an indirect to a direct bandgap for mono- and bi-layers of MoS_2 on Si/SiO_2 substrates.

In this thesis, the chemical and electronic properties of a 2H phase MoS_2 single crystal were investigated using a wide variety of photoelectron and soft x-ray spectroscopic techniques, complemented with theoretical calculations of the band structure and low-energy electron diffraction measurements. This was done in hopes of providing information to further understand and optimize the material.

Chapter 3 explored the chemical structure of an as-received 2H phase MoS_2 single crystal and one that underwent mechanical exfoliation using the adhesive tape method. Mechanical exfoliation was tested as a way to remove surface adsorbates and contaminants and to see how effectively the exfoliation removed flat layers of the single crystal. To see the effects of the mechanical exfoliation and to verify the surface composition and 2H phase of MoS_2, XPS and XAES were employed. Using these techniques, it was found that the exfoliation reduced, but did not fully remove the carbon and oxygen signals, while increasing the detected signal of Mo- and S-related peaks. The surface of this highly ordered crystal, both before and after the exfoliation, has high amounts of carbon, which can be more readily seen after accounting for variations in the intensity contributions for the prevalent photoelectron lines. While carbon saw a significant change in its measured intensity after the exfoliation, oxygen-related peaks did not vary substantially; the detected Mo- and S-related peaks increased in intensity. The surface stoichiometry of the exfoliated surface for C : O : Mo : S was found to be 25% : 3% : 22% : 50%, indicating the prevalence of carbon on the surface (and thus likely also in the bulk) of the sample. The S/Mo ratio was derived at 2.00 ± 0.02, similar to previous photoelectron studies of the 2H MoS_2 surface and indicated the possibility of molybdenum vacancies. Finally, LEED was used and discussed in this chapter mostly to help verify the 2H phase of the sample and assess how the lattice structure was effected by surface contaminations. The LEED images, measured with a 60 eV bias voltage showed a well-ordered honeycomb structure associated with the 2H phase.

These results were corroborated with information about the electronic structure using both lab-based and synchrotron-based techniques in Chapter 4. To start off the discussion, a comparison of the valence band structure measured between various techniques was conducted. The effects of mechanical exfoliation were also analyzed using UPS, where it was found that the tape method results in an increase of the derived work function from 4.39 to 4.89 (± 0.10) eV. The valence band features measured with He I UPS became enhanced after the exfoliation and the linearly extrapolated VBM was found at 0.63 ± 0.10 eV and shifted to 0.82 ± 0.10 eV. Combined with IPES, a surface bandgap value of an exfoliated 2H phase MoS_2 was found between 1.00 and 1.13 eV, within the confidence range of ± 0.14 eV. Bandgap values from RIXS maps were also derived, with a direct bandgap at the CBM was found at 1.66 eV using the highest emission energy for lowest excitation energy. In addition, the direct bandgap at the VBM was derived at 1.87 eV. The band dispersion located within the resonant portion of the RIXS map was also analyzed and compared to possible band contributions from a calculated band structure.

In future work, there is much that can be done to gain a deeper understanding of MoS_2 and other TMDCs. This includes testing the effects of other exfoliation techniques as well as surface cleaning techniques, including the effects of ion treating and ion sputtering, and annealing of the single crystal on its surface chemical and electronic properties. Using this toolchest of spectroscopic techniques for the other TMDC materials or the different phases of MoS_2 especially would be of great value, particularly with RIXS. Making more use of techniques like LEED to also derive the experimental lattice parameters and perhaps use those to aid in theoretical calculations of the electronic structure that currently used only theoretical parameters.

APPENDIX

Appendix A: Deriving concentration ratios of elements

To derive the concentration ratio between various photoelectron lines measured with XPS, as done in Section 3.2.1, the following equation can be used:

$$\frac{c_A}{c_B} = \frac{I_A \cdot \ \sigma_B \cdot \lambda_B(E_{Kin}) \cdot T\left(E_{Kin,B}\right)}{I_B \cdot \ \sigma_A \cdot \lambda_A(E_{Kin}) \cdot T\left(E_{Kin,A}\right)}$$

Where the photoionization cross-sections of investigated transition (σ_x), inelastic mean free paths (λ_x), and transmission function of the analyzer (T_x) were considered when deriving the concentration ratio between elements.

As mentioned, the photoionization cross-sections used in this study were determined by J. H. Scofield in reference [64], while the inelastic mean free path was determined with the QUASES software.[63] The transmission function of the Scienta R4000 electron analyzer was conducted by collecting a survey spectrum of a clean Ag foil at each pass energy utilized in this study (for XPS data used to derive the concentration ratios, a pass energy of 100 eV was used for each region). The reference spectrum was then fitted according to references [126,127] in order to account for intensity distortions caused by the magnetic fields and internal scattering within the analyzer.

REFERENCES

(1) Wilson, J. A.; Yoffe, A. D. The Transition Metal Dichalcogenides Discussion and Interpretation of the Observed Optical, Electrical and Structural Properties. *Advances in Physics* **1969**, *18* (73), 193–335. https://doi.org/10.1080/00018736900101307.

(2) Coehoorn, R.; Haas, C.; Dijkstra, J.; Flipse, C. J. F.; de Groot, R. A.; Wold, A. Electronic Structure of $MoSe_2$, MoS_2, and WSe_2 . I. Band-Structure Calculations and Photoelectron Spectroscopy. *Phys. Rev. B* **1987**, *35* (12), 6195–6202. https://doi.org/10.1103/PhysRevB.35.6195.

(3) Gao, G.; Jiao, Y.; Ma, F.; Jiao, Y.; Waclawik, E.; Du, A. Charge Mediated Semiconducting-to-Metallic Phase Transition in Molybdenum Disulfide Monolayer and Hydrogen Evolution Reaction in New 1T′ Phase. *J. Phys. Chem. C* **2015**, *119* (23), 13124–13128. https://doi.org/10.1021/acs.jpcc.5b04658.

(4) Gan, X.; Lee, L. Y. S.; Wong, K.; Lo, T. W.; Ho, K. H.; Lei, D. Y.; Zhao, H. 2H/1T Phase Transition of Multilayer MoS_2 by Electrochemical Incorporation of S Vacancies. *ACS Appl. Energy Mater.* **2018**, *1* (9), 4754–4765. https://doi.org/10.1021/acsaem.8b00875.

(5) Samy, O.; Zeng, S.; Birowosuto, M. D.; El Moutaouakil, A. A Review on MoS_2 Properties, Synthesis, Sensing Applications and Challenges. *Crystals* **2021**, *11* (4), 355. https://doi.org/10.3390/cryst11040355.

(6) Manzeli, S.; Ovchinnikov, D.; Pasquier, D.; Yazyev, O. V.; Kis, A. 2D Transition Metal Dichalcogenides. *Nat Rev Mater* **2017**, *2* (8), 17033. https://doi.org/10.1038/natrevmats.2017.33.

(7) Baik, S. S.; Im, S.; Choi, H. J. Work Function Tuning in Two-Dimensional MoS_2 Field-Effect-Transistors with Graphene and Titanium Source-Drain Contacts. *Sci Rep* **2017**, *7* (1), 45546. https://doi.org/10.1038/srep45546.

(8) Mak, K. F.; Lee, C.; Hone, J.; Shan, J.; Heinz, T. F. Atomically Thin MoS_2: A New Direct-Gap Semiconductor. *Phys. Rev. Lett.* **2010**, *105* (13), 136805. https://doi.org/10.1103/PhysRevLett.105.136805.

(9) Splendiani, A.; Sun, L.; Zhang, Y.; Li, T.; Kim, J.; Chim, C.-Y.; Galli, G.; Wang, F. Emerging Photoluminescence in Monolayer MoS_2. *Nano Lett.* **2010**, *10* (4), 1271–1275. https://doi.org/10.1021/nl903868w.

(10) Jin, W.; Yeh, P.-C.; Zaki, N.; Zhang, D.; Sadowski, J. T.; Al-Mahboob, A.; van der Zande, A. M.; Chenet, D. A.; Dadap, J. I.; Herman, I. P.; Sutter, P.; Hone, J.; Osgood, R. M. Direct Measurement of the Thickness-Dependent Electronic Band Structure of MoS_2 Using Angle-Resolved Photoemission Spectroscopy. *Phys. Rev. Lett.* **2013**, *111* (10), 106801. https://doi.org/10.1103/PhysRevLett.111.106801.

(11) Dai, Z.; Jin, W.; Grady, M.; Sadowski, J. T.; Dadap, J. I.; Osgood, R. M.; Pohl, K. Surface Structure of Bulk 2H-MoS_2(0001) and Exfoliated Suspended Monolayer MoS_2: A Selected Area Low Energy Electron Diffraction Study. *Surface Science* **2017**, *660*, 16–21. https://doi.org/10.1016/j.susc.2017.02.005.

(12) Hussain, S.; Singh, J.; Vikraman, D.; Singh, A. K.; Iqbal, M. Z.; Khan, M. F.; Kumar, P.; Choi, D.-C.; Song, W.; An, K.-S.; Eom, J.; Lee, W.-G.; Jung, J. Large-Area, Continuous and High Electrical Performances of Bilayer to Few Layers MoS_2 Fabricated by RF Sputtering via Post-Deposition Annealing Method. *Sci Rep* **2016**, *6* (1), 30791. https://doi.org/10.1038/srep30791.

(13) Chowdhury, T.; Sadler, E. C.; Kempa, T. J. Progress and Prospects in Transition-Metal Dichalcogenide Research Beyond 2D. *Chem. Rev.* **2020**, *120* (22), 12563–12591. https://doi.org/10.1021/acs.chemrev.0c00505.

(14) Li, Y.; Chang, K.; Sun, Z.; Shangguan, E.; Tang, H.; Li, B.; Sun, J.; Chang, Z. Selective Preparation of 1T- and 2H-Phase MoS_2 Nanosheets with Abundant Monolayer Structure and Their Applications in Energy Storage Devices. *ACS Appl. Energy Mater.* **2020**, *3* (1), 998–1009. https://doi.org/10.1021/acsaem.9b02043.

(15) Magda, G. Z.; Pető, J.; Dobrik, G.; Hwang, C.; Biró, L. P.; Tapasztó, L. Exfoliation of Large-Area Transition Metal Chalcogenide Single Layers. *Sci Rep* **2015**, *5* (1), 14714. https://doi.org/10.1038/srep14714.

(16) Huang, Y.; Pan, Y.-H.; Yang, R.; Bao, L.-H.; Meng, L.; Luo, H.-L.; Cai, Y.-Q.; Liu, G.-D.; Zhao, W.-J.; Zhou, Z.; Wu, L.-M.; Zhu, Z.-L.; Huang, M.; Liu, L.-W.; Liu, L.; Cheng, P.; Wu, K.-H.; Tian, S.-B.; Gu, C.-Z.; Shi, Y.-G.; Guo, Y.-F.; Cheng, Z. G.; Hu, J.-P.; Zhao, L.; Yang, G.-H.; Sutter, E.; Sutter, P.; Wang, Y.-L.; Ji, W.; Zhou, X.-J.; Gao, H.-J. Universal Mechanical Exfoliation of Large-Area 2D Crystals. *Nat Commun* **2020**, *11* (1), 2453. https://doi.org/10.1038/s41467-020-16266-w.

(17) Li, H.; Wu, J.; Yin, Z.; Zhang, H. Preparation and Applications of Mechanically Exfoliated Single-Layer and Multilayer MoS_2 and WSe_2 Nanosheets. *Acc. Chem. Res.* **2014**, *47* (4), 1067–1075. https://doi.org/10.1021/ar4002312.

(18) Hüfner, S. *Photoelectron Spectroscopy*; Advanced Texts in Physics; Springer Berlin Heidelberg: Berlin, Heidelberg, 2003.

(19) Moulder, J.; Stickle, W.; Sobol, W.; Bomben, K. D. *Handbook of X-Ray Photoelectron Spectroscopy: A Reference Book of Standard Spectra for Identification and Interpretation of XPS Data*; Perkin-Elmer Corporation.; Physical Electronics Division: Eden Prairie, MN, 1992.

(20) Briggs, D.; Seah, M. P. *Practical Surface Analysis by Auger and X-Ray Photoelectron Spectroscopy.*; Wiley: Chichester, 1983.

(21) Persson, P.; Lunell, S.; Szöke, A.; Ziaja, B.; Hajdu, J. Shake-up and Shake-off Excitations with Associated Electron Losses in X-Ray Studies of Proteins. *Protein Science* **2001**, *10* (12), 2480–2484. https://doi.org/10.1110/ps.ps.26201.

(22) Smith, N. V. Inverse Photoemission. *Rep. Prog. Phys.* **1988**, *51* (9), 1227. https://doi.org/10.1088/0034-4885/51/9/003.

(23) Gleim, Th.; Heske, C.; Umbach, E.; Schumacher, C.; Faschinger, W.; Ammon, Ch.; Probst, M.; Steinrück, H.-P. Reduction of the ZnSe/GaAs(100) Valence Band Offset by a Te Interlayer. *Applied Physics Letters* **2001**, *78* (13), 1867–1869. https://doi.org/10.1063/1.1358366.

(24) Gleim, T.; Heske, C.; Umbach, E.; Schumacher, C.; Gundel, S.; Faschinger, W.; Fleszar, A.; Ammon, C.; Probst, M.; Steinrück, H.-P. Formation of the ZnSe/(Te/)GaAs(100) Heterojunction. *Surface Science* **2003**, *531* (1), 77–85. https://doi.org/10.1016/S0039-6028(03)00439-4.

(25) Eich, D.; Ortner, K.; Groh, U.; Chen, Z. H.; Becker, C. R.; Landwehr, G.; Fink, R.; Umbach, E. Band Discontinuity and Band Gap of MBE Grown HgTe/CdTe(001) Heterointerfaces Studied by k-Resolved Photoemission and Inverse Photoemission. *phys. stat. sol. (a)* **1999**, *173* (1), 261–267. https://doi.org/10.1002/(SICI)1521-396X(199905)173:1<261::AID-PSSA261>3.0.CO;2-#.

(26) Dirac, P. A. M. The Quantum Theory of the Emission and Absorption of Radiation. *Proceedings of the Royal Society of London. Series A* **1927**, *114* (767). https://doi.org/10.1098/rspa.1927.0039.

(27) Fuchs, O. Soft X-Ray Spectroscopy of Organic Molecules and Liquids, Universität Würzburg, 2009.

(28) Ma, Y.; Wassdahl, N.; Skytt, P.; Guo, J.; Nordgren, J.; Johnson, P. D.; Rubensson, J.-E.; Boske, T.; Eberhardt, W.; Kevan, S. D. Soft-x-Ray Resonant Inelastic Scattering at the C *K* Edge of Diamond. *Phys. Rev. Lett.* **1992**, *69* (17), 2598–2601. https://doi.org/10.1103/PhysRevLett.69.2598.

(29) Fermi, E. *Nuclear Physics.*; University of Chicago Press: Chicago, IL, 1950.

(30) Mahan, G. D. Final-State Potential in x-Ray Spectra. *Phys. Rev. B* **1980**, *21* (4), 1421–1431. https://doi.org/10.1103/PhysRevB.21.1421.

(31) Rubensson, J.-E.; Lüning, J.; Eisebitt, S.; Eberhardt, W. It's Always a One-Step Process. *Applied Physics A: Materials Science & Processing* **1997**, *65* (2), 91–96. https://doi.org/10.1007/s003390050549.

(32) Ma, Y. X-Ray Absorption, Emission, and Resonant Inelastic Scattering in Solids. *Phys. Rev. B* **1994**, *49* (9), 5799–5805. https://doi.org/10.1103/PhysRevB.49.5799.

(33) Rubensson, J.-E.; Wassdahl, N.; Bray, G.; Rindstedt, J.; Nyholm, R.; Cramm, S.; Mårtensson, N.; Nordgren, J. Resonant Behavior in Soft X-Ray Fluorescence Excited by Monochromatized Synchrotron Radiation. *Phys. Rev. Lett.* **1988**, *60* (17), 1759–1762. https://doi.org/10.1103/PhysRevLett.60.1759.

(34) Rubensson, J.-E. RIXS Dynamics for Beginners. *Journal of Electron Spectroscopy and Related Phenomena* **2000**, *110–111*, 135–151. https://doi.org/10.1016/S0368-2048(00)00161-4.

(35) Eisebitt, S.; Eberhardt, W. Band Structure Information and Resonant Inelastic Soft X-Ray Scattering in Broad Band Solids. *Journal of Electron Spectroscopy and Related Phenomena* **2000**, *110–111*, 335–358. https://doi.org/10.1016/S0368-2048(00)00172-9.

(36) Kramers, H. A.; Heisenberg, W. Über die Streuung von Strahlung durch Atome. *Z. Physik* **1925**, *31* (1), 681–708. https://doi.org/10.1007/BF02980624.

(37) Weisskopf, V.; Wigner, E. Berechnung der natürlichen Linienbreite auf Grund der Diracschen Lichttheorie. *Z. Physik* **1930**, *63* (1), 54–73. https://doi.org/10.1007/BF01336768.

(38) Iwasawa, H. High-Resolution Angle-Resolved Photoemission Spectroscopy and Microscopy. *Electron. Struct.* **2020**, *2* (4), 043001. https://doi.org/10.1088/2516-1075/abb379.

(39) Gauthier, N.; Sobota, J. A.; Pfau, H.; Gauthier, A.; Soifer, H.; Bachmann, M. D.; Fisher, I. R.; Shen, Z.-X.; Kirchmann, P. S. Expanding the Momentum Field of View in Angle-Resolved Photoemission Systems with Hemispherical Analyzers. *Review of Scientific Instruments* **2021**, *92* (12), 123907. https://doi.org/10.1063/5.0053479.

(40) Van Hove, M. A.; Tong, S. Y. *Surface Crystallography by LEED*; Goldanskii, V. I., Gomer, R., Schäfer, F. P., Toennies, J. P., Series Eds.; Springer Series in Chemical Physics; Springer Berlin Heidelberg: Berlin, Heidelberg, 1979; Vol. 2. https://doi.org/10.1007/978-3-642-67195-1.

(41) Zhao, W.; Xia, B.; Lin, L.; Xiao, X.; Liu, P.; Lin, X.; Peng, H.; Zhu, Y.; Yu, R.; Lei, P.; Wang, J.; Zhang, L.; Xu, Y.; Zhao, M.; Peng, L.; Li, Q.; Duan, W.; Liu, Z.; Fan, S.; Jiang, K. Low-Energy Transmission Electron Diffraction and Imaging of Large-Area Graphene. *Sci. Adv.* **2017**, *3* (9), e1603231. https://doi.org/10.1126/sciadv.1603231.

(42) Prutton, M. Low Energy Electron Diffraction. *Science Progress (1933-)* **1978**, *65* (258), 209–229.

(43) Yoshida, H. Near-Ultraviolet Inverse Photoemission Spectroscopy Using Ultra-Low Energy Electrons. *Chemical Physics Letters* **2012**, *539–540*, 180–185. https://doi.org/10.1016/j.cplett.2012.04.058.

(44) Blum, M.; Weinhardt, L.; Fuchs, O.; Bär, M.; Zhang, Y.; Weigand, M.; Krause, S.; Pookpanratana, S.; Hofmann, T.; Yang, W.; Denlinger, J. D.; Umbach, E.; Heske, C. Solid and Liquid Spectroscopic Analysis (SALSA)–a Soft x-Ray Spectroscopy Endstation with a Novel Flow-through Liquid Cell. *Review of Scientific Instruments* **2009**, *80* (12), 123102. https://doi.org/10.1063/1.3257926.

(45) Blaha, P.; Schwarz, K.; Tran, F.; Laskowski, R.; Madsen, G. K. H.; Marks, L. D. WIEN2k: An APW+lo Program for Calculating the Properties of Solids. *The Journal of Chemical Physics* **2020**, *152* (7), 074101. https://doi.org/10.1063/1.5143061.

(46) Perdew, J. P.; Burke, K.; Ernzerhof, M. Generalized Gradient Approximation Made Simple. *Phys. Rev. Lett.* **1996**, *77* (18), 3865–3868. https://doi.org/10.1103/PhysRevLett.77.3865.

(47) Jain, A.; Ong, S. P.; Hautier, G.; Chen, W.; Richards, W. D.; Dacek, S.; Cholia, S.; Gunter, D.; Skinner, D.; Ceder, G.; Persson, K. A. Commentary: The Materials Project: A Materials Genome Approach to Accelerating Materials Innovation. *APL Materials* **2013**, *1* (1), 011002. https://doi.org/10.1063/1.4812323.

(48) Ahmad, S.; Mukherjee, S. A Comparative Study of Electronic Properties of Bulk MoS_2 and Its Monolayer Using DFT Technique: Application of Mechanical Strain on MoS_2 Monolayer. *Graphene* **2014**, *03* (04), 52–59. https://doi.org/10.4236/graphene.2014.34008.

(49) Mattheiss, L. F. Band Structures of Transition-Metal-Dichalcogenide Layer Compounds. *Phys. Rev. B* **1973**, *8* (8), 3719–3740. https://doi.org/10.1103/PhysRevB.8.3719.

(50) Kertesz, M.; Hoffmann, R. Octahedral vs. Trigonal-Prismatic Coordination and Clustering in Transition-Metal Dichalcogenides. *J. Am. Chem. Soc.* **1984**, *106* (12), 3453–3460. https://doi.org/10.1021/ja00324a012.

(51) Nassiri Nazif, K.; Daus, A.; Hong, J.; Lee, N.; Vaziri, S.; Kumar, A.; Nitta, F.; Chen, M. E.; Kananian, S.; Islam, R.; Kim, K.-H.; Park, J.-H.; Poon, A. S. Y.; Brongersma, M. L.; Pop, E.; Saraswat, K. C. High-Specific-Power Flexible Transition Metal Dichalcogenide Solar Cells. *Nat Commun* **2021**, *12* (1), 7034. https://doi.org/10.1038/s41467-021-27195-7.

(52) Aftab, S.; Iqbal, M. Z.; Hussain, S.; Hegazy, H. H.; Saeed, M. A. Transition Metal Dichalcogenides Solar Cells and Integration with Perovskites. *Nano Energy* **2023**, *108*, 108249. https://doi.org/10.1016/j.nanoen.2023.108249.

(53) Dickinson, R. G.; Pauling, L. The Crystal Structure of Molybdenite. *J. Am. Chem. Soc.* **1923**, *45* (6), 1466–1471. https://doi.org/10.1021/ja01659a020.

(54) Yoon, J.; Park, W.; Bae, G.; Kim, Y.; Jang, H. S.; Hyun, Y.; Lim, S. K.; Kahng, Y. H.; Hong, W.; Lee, B. H.; Ko, H. C. Highly Flexible and Transparent Multilayer MoS_2 Transistors with Graphene Electrodes. *Small* **2013**, *9* (19), 3295–3300. https://doi.org/10.1002/smll.201300134.

(55) *Synthetic Molybdenum Disulfide (MoS_2)*. 2D Semiconductors. https://www.2dsemiconductors.com/synthetic-molybdenum-disulfide-mos2/ (accessed 2023-09-10).

(56) Coleman, J. N.; Lotya, M.; O'Neill, A.; Bergin, S. D.; King, P. J.; Khan, U.; Young, K.; Gaucher, A.; De, S.; Smith, R. J.; Shvets, I. V.; Arora, S. K.; Stanton, G.; Kim, H.-Y.; Lee, K.; Kim, G. T.; Duesberg, G. S.; Hallam, T.; Boland, J. J.; Wang, J. J.; Donegan, J. F.; Grunlan, J. C.; Moriarty, G.; Shmeliov, A.; Nicholls, R. J.; Perkins, J. M.; Grieveson, E. M.; Theuwissen, K.; McComb, D. W.; Nellist, P. D.; Nicolosi, V. Two-Dimensional Nanosheets Produced by Liquid Exfoliation of Layered Materials. *Science* **2011**, *331* (6017), 568–571. https://doi.org/10.1126/science.1194975.

(57) Momma, K.; Izumi, F. VESTA 3 for Three-Dimensional Visualization of Crystal, Volumetric and Morphology Data. *J Appl Cryst* **2011**, *44* (6), 1272–1276. https://doi.org/10.1107/S0021889811038970.

(58) Böker, Th.; Severin, R.; Müller, A.; Janowitz, C.; Manzke, R.; Voß, D.; Krüger, P.; Mazur, A.; Pollmann, J. Band Structure of MoS_2, $MoSe_2$, and A−$MoTe_2$: Angle-Resolved Photoelectron Spectroscopy and *Ab Initio* Calculations. *Phys. Rev. B* **2001**, *64* (23), 235305. https://doi.org/10.1103/PhysRevB.64.235305.

(59) Cattelan, M.; Fox, N. A Perspective on the Application of Spatially Resolved ARPES for 2D Materials. *Nanomaterials* **2018**, *8* (5), 284. https://doi.org/10.3390/nano8050284.

(60) Damascelli, A. Probing the Electronic Structure of Complex Systems by ARPES. *Physica Scripta* **2004**, *T109*, 61. https://doi.org/10.1238/Physica.Topical.109a00061.

(61) Ganta, D.; Sinha, S.; Haasch, R. T. 2-D Material Molybdenum Disulfide Analyzed by XPS. *Surface Science Spectra* **2014**, *21* (1), 19–27. https://doi.org/10.1116/11.20140401.

(62) Moynihan, E.; Rost, S.; O'connell, E.; Ramasse, Q.; Friedrich, C.; Bangert, U. Plasmons in MoS_2 Studied via Experimental and Theoretical Correlation of Energy

Loss Spectra. *Journal of Microscopy* **2020**, *279* (3), 256–264. https://doi.org/10.1111/jmi.12900.

(63) *QUASES-IMFP-TPP2M - QUASES*. http://www.quases.com/products/quases-imfp-tpp2m/ (accessed 2023-09-18).

(64) Scofield, J. H. Hartree-Slater Subshell Photoionization Cross-Sections at 1254 and 1487 EV. *Journal of Electron Spectroscopy and Related Phenomena* **1976**, *8* (2), 129–137. https://doi.org/10.1016/0368-2048(76)80015-1.

(65) Hauschild, D.; Wachs, S. J.; Kogler, W.; Seitz, L.; Carter, J.; Schnabel, T.; Krause, B.; Blum, M.; Yang, W.; Ahlswede, E.; Heske, C.; Weinhardt, L. Chemical Structure of a Carbon-Rich Layer at the Wet-Chemical Processed $Cu_2ZnSn(S,Se)_4$/Mo Interface. *IEEE J. Photovoltaics* **2021**, *11* (3), 658–663. https://doi.org/10.1109/JPHOTOV.2021.3059423.

(66) Xi, J.; Huang, X.; Hu, M.; Xiang, W. Dependence of Laser Parameters on Structural Properties of Pulsed Laser-Deposited MoS_2 Thin Films Applicable for Field Effect Transistors. *J Mater Sci: Mater Electron* **2020**, *31* (23), 21118–21127. https://doi.org/10.1007/s10854-020-04624-9.

(67) Park, S. J.; Chu, D.; Kim, E. K. Controllable Growth of Single Layer MoS_2 and Resistance Switching Effect in Polymer/MoS_2 Structure. *Appl. Sci. Converg. Technol.* **2017**, *26* (5), 129–132. https://doi.org/10.5757/ASCT.2017.26.5.129.

(68) Timpel, M.; Ligorio, G.; Ghiami, A.; Gavioli, L.; Cavaliere, E.; Chiappini, A.; Rossi, F.; Pasquali, L.; Gärisch, F.; List-Kratochvil, E. J. W.; Nozar, P.; Quaranta, A.; Verucchi, R.; Nardi, M. V. 2D-MoS_2 Goes 3D: Transferring Optoelectronic Properties of 2D MoS_2 to a Large-Area Thin Film. *npj 2D Mater Appl* **2021**, *5* (1), 64. https://doi.org/10.1038/s41699-021-00244-x.

(69) Zhang, R.; Li, Y.; Qi, J.; Gao, D. Ferromagnetism in Ultrathin MoS_2 Nanosheets: From Amorphous to Crystalline. *Nanoscale Res Lett* **2014**, *9* (1), 586. https://doi.org/10.1186/1556-276X-9-586.

(70) Silambarasan, K.; Archana, J.; Harish, S.; Navaneethan, M.; Sankar Ganesh, R.; Ponnusamy, S.; Muthamizhchelvan, C.; Hara, K. One-Step Fabrication of Ultrathin Layered 1T@2H Phase MoS_2 with High Catalytic Activity Based Counter Electrode for Photovoltaic Devices. *Journal of Materials Science & Technology* **2020**, *51*, 94–101. https://doi.org/10.1016/j.jmst.2020.01.024.

(71) Lin, Q.; Dong, X.; Wang, Y.; Zheng, N.; Zhao, Y.; Xu, W.; Ding, T. Molybdenum Disulfide with Enlarged Interlayer Spacing Decorated on Reduced Graphene Oxide for Efficient Electrocatalytic Hydrogen Evolution. *J Mater Sci* **2020**, *55* (15), 6637–6647. https://doi.org/10.1007/s10853-020-04478-w.

(72) Li, F.; Zhang, L.; Li, J.; Lin, X.; Li, X.; Fang, Y.; Huang, J.; Li, W.; Tian, M.; Jin, J.; Li, R. Synthesis of Cu–MoS_2/RGO Hybrid as Non-Noble Metal Electrocatalysts for the Hydrogen Evolution Reaction. *Journal of Power Sources* **2015**, *292*, 15–22. https://doi.org/10.1016/j.jpowsour.2015.04.173.

(73) Yan, Y.; Ge, X.; Liu, Z.; Wang, J.-Y.; Lee, J.-M.; Wang, X. Facile Synthesis of Low Crystalline MoS_2 Nanosheet-Coated CNTs for Enhanced Hydrogen Evolution Reaction. *Nanoscale* **2013**, *5* (17), 7768. https://doi.org/10.1039/c3nr02994h.

(74) Xiong, X.; Luo, W.; Hu, X.; Chen, C.; Qie, L.; Hou, D.; Huang, Y. Flexible Membranes of MoS_2/C Nanofibers by Electrospinning as Binder-Free Anodes for High-Performance Sodium-Ion Batteries. *Sci Rep* **2015**, *5* (1), 9254. https://doi.org/10.1038/srep09254.

(75) Ghiami, A.; Timpel, M.; Nardi, M. V.; Chiappini, A.; Nozar, P.; Quaranta, A.; Verucchi, R. Unravelling Work Function Contributions and Their Engineering in 2H-MoS_2 Single Crystal Discovered by Molecular Probe Interaction. *J. Phys. Chem. C* **2020**, *124* (12), 6732–6740. https://doi.org/10.1021/acs.jpcc.0c00733.

(76) Mitterreiter, E.; Schuler, B.; Micevic, A.; Hernangómez-Pérez, D.; Barthelmi, K.; Cochrane, K. A.; Kiemle, J.; Sigger, F.; Klein, J.; Wong, E.; Barnard, E. S.; Watanabe, K.; Taniguchi, T.; Lorke, M.; Jahnke, F.; Finley, J. J.; Schwartzberg, A. M.; Qiu, D. Y.; Refaely-Abramson, S.; Holleitner, A. W.; Weber-Bargioni, A.; Kastl, C. The Role of Chalcogen Vacancies for Atomic Defect Emission in MoS_2. *Nat Commun* **2021**, *12* (1), 3822. https://doi.org/10.1038/s41467-021-24102-y.

(77) Naumkin, A. V.; Kraut-Vass, A.; Gaarenstroom, S. W.; Powell, C. J. NIST X-Ray Photoelectron Spectroscopy Database, NIST Standard Reference Database Number 20. https://srdata.nist.gov/xps/Default.aspx (accessed 2023-03-28).

(78) Hauschild, D.; Meyer, F.; Pohlner, S.; Lechner, R.; Dietmüller, R.; Palm, J.; Heske, C.; Weinhardt, L.; Reinert, F. Impact of Environmental Conditions on the Chemical Surface Properties of Cu(In,Ga)$(S,Se)_2$ Thin-Film Solar Cell Absorbers. *Journal of Applied Physics* **2014**, *115* (18), 183707. https://doi.org/10.1063/1.4876257.

(79) Weinhardt, L.; Fuchs, O.; Groß, D.; Umbach, E.; Heske, C.; Dhere, N. G.; Kadam, A. A.; Kulkarni, S. S. Surface Modifications of Cu(In,Ga)S_2 Thin Film Solar Cell Absorbers by KCN and H_2O_2/H_2SO_4 Treatments. *Journal of Applied Physics* **2006**, *100* (2), 024907. https://doi.org/10.1063/1.2216367.

(80) Hao, S.; Yang, B.; Gao, Y. Chemical Vapor Deposition Growth and Characterization of Drop-like MoS_2/MoO_2 Granular Films: CVD Growth and Characterization of Drop-like MoS_2/MoO_2 Granular Films. *Phys. Status Solidi B* **2017**, *254* (4), 1600245. https://doi.org/10.1002/pssb.201600245.

(81) Fleischauer, P. D.; Lince, J. R. A Comparison of Oxidation and Oxygen Substitution in MoS_2 Solid Film Lubricants. *Tribology International* **1999**, *32* (11), 627–636. https://doi.org/10.1016/S0301-679X(99)00088-2.

(82) Wojdyr, M. Fityk: A General-Purpose Peak Fitting Program. *J Appl Cryst* **2010**, *43* (5), 1126–1128. https://doi.org/10.1107/S0021889810030499.

(83) Zhang, C.; Wang, Z.; Bhoyate, S.; Morey, T.; Neria, B.; Vasiraju, V.; Gupta, G.; Palchoudhury, S.; Kahol, P.; Mishra, S.; Perez, F.; Gupta, R. MoS2 Decorated Carbon Nanofibers as Efficient and Durable Electrocatalyst for Hydrogen Evolution Reaction. *C* **2017**, *3* (4), 33. https://doi.org/10.3390/c3040033.

(84) Lee, W.; Lin, Y.; Lu, L.-S.; Chueh, W.-C.; Liu, M.; Li, X.; Chang, W.-H.; Kaindl, R. A.; Shih, C.-K. Time-Resolved ARPES Determination of a Quasi-Particle Band Gap and Hot Electron Dynamics in Monolayer MoS_2. *Nano Lett.* **2021**, *21* (17), 7363–7370. https://doi.org/10.1021/acs.nanolett.1c02674.

(85) Yu, H.; Liao, M.; Zhao, W.; Liu, G.; Zhou, X. J.; Wei, Z.; Xu, X.; Liu, K.; Hu, Z.; Deng, K.; Zhou, S.; Shi, J.-A.; Gu, L.; Shen, C.; Zhang, T.; Du, L.; Xie, L.; Zhu, J.; Chen, W.; Yang, R.; Shi, D.; Zhang, G. Wafer-Scale Growth and Transfer of Highly-Oriented Monolayer MoS_2 Continuous Films. *ACS Nano* **2017**, *11* (12), 12001–12007. https://doi.org/10.1021/acsnano.7b03819.

(86) Komesu, T.; Le, D.; Ma, Q.; Schwier, E. F.; Kojima, Y.; Zheng, M.; Iwasawa, H.; Shimada, K.; Taniguchi, M.; Bartels, L.; Rahman, T. S.; Dowben, P. A. Symmetry-Resolved Surface-Derived Electronic Structure of MoS_2 (0001). *J. Phys.: Condens. Matter* **2014**, *26* (45), 455501. https://doi.org/10.1088/0953-8984/26/45/455501.

(87) Mahatha, S. K.; Patel, K. D.; Menon, K. S. R. Electronic Structure Investigation of MoS_2 and $MoSe_2$ Using Angle-Resolved Photoemission Spectroscopy and *Ab Initio*

Band Structure Studies. *J. Phys.: Condens. Matter* **2012**, *24* (47), 475504. https://doi.org/10.1088/0953-8984/24/47/475504.

(88) Weinhardt, L.; Hauschild, D.; Steininger, R.; Jiang, N.; Blum, M.; Yang, W.; Heske, C. Sulfate Speciation Analysis Using Soft X-Ray Emission Spectroscopy. *Anal. Chem.* **2021**, *93* (23), 8300–8308. https://doi.org/10.1021/acs.analchem.1c01187.

(89) Lin, J.; Zhong, J.; Zhong, S.; Li, H.; Zhang, H.; Chen, W. Modulating Electronic Transport Properties of MoS_2 Field Effect Transistor by Surface Overlayers. *Applied Physics Letters* **2013**, *103* (6), 063109. https://doi.org/10.1063/1.4818463.

(90) Ochedowski, O.; Marinov, K.; Scheuschner, N.; Poloczek, A.; Bussmann, B. K.; Maultzsch, J.; Schleberger, M. Effect of Contaminations and Surface Preparation on the Work Function of Single Layer MoS_2. *Beilstein J. Nanotechnol.* **2014**, *5*, 291–297. https://doi.org/10.3762/bjnano.5.32.

(91) Makarova, M.; Okawa, Y.; Aono, M. Selective Adsorption of Thiol Molecules at Sulfur Vacancies on MoS_2 (0001), Followed by Vacancy Repair via S–C Dissociation. *J. Phys. Chem. C* **2012**, *116* (42), 22411–22416. https://doi.org/10.1021/jp307267h.

(92) Zhang, H.; Pincelli, T.; Jozwiak, C.; Kondo, T.; Ernstorfer, R.; Sato, T.; Zhou, S. Angle-Resolved Photoemission Spectroscopy. *Nat Rev Methods Primers* **2022**, *2* (1), 54. https://doi.org/10.1038/s43586-022-00133-7.

(93) Lv, B. Q.; Qian, T.; Ding, H. Angle-Resolved Photoemission Spectroscopy and Its Applications to Topological Materials.

(94) Kim, B. S.; Rhim, J.-W.; Kim, B.; Kim, C.; Park, S. R. Determination of the Band Parameters of Bulk 2H-MX_2(M=Mo, W; X=S, Se) by Angle-Resolved Photoemission Spectroscopy. *Sci Rep* **2016**, *6* (1), 36389. https://doi.org/10.1038/srep36389.

(95) Han, S. W.; Cha, G.-B.; Frantzeskakis, E.; Razado-Colambo, I.; Avila, J.; Park, Y. S.; Kim, D.; Hwang, J.; Kang, J. S.; Ryu, S.; Yun, W. S.; Hong, S. C.; Asensio, M. C. Band-Gap Expansion in the Surface-Localized Electronic Structure of MoS_2 (0002). *Phys. Rev. B* **2012**, *86* (11), 115105. https://doi.org/10.1103/PhysRevB.86.115105.

(96) Gehlmann, M.; Aguilera, I.; Bihlmayer, G.; Młyńczak, E.; Eschbach, M.; Döring, S.; Gospodarič, P.; Cramm, S.; Kardynał, B.; Plucinski, L.; Blügel, S.; Schneider, C. M.

Quasi 2D Electronic States with High Spin-Polarization in Centrosymmetric MoS_2 Bulk Crystals. *Sci Rep* **2016**, *6* (1), 26197. https://doi.org/10.1038/srep26197.

(97) Jin, W.; Yeh, P.-C.; Zaki, N.; Zhang, D.; Liou, J. T.; Sadowski, J. T.; Barinov, A.; Yablonskikh, M.; Dadap, J. I.; Sutter, P.; Herman, I. P.; Osgood, R. M. Substrate Interactions with Suspended and Supported Monolayer MoS_2: Angle-Resolved Photoemission Spectroscopy. *Phys. Rev. B* **2015**, *91* (12), 121409. https://doi.org/10.1103/PhysRevB.91.121409.

(98) Scheuschner, N.; Ochedowski, O.; Kaulitz, A.-M.; Gillen, R.; Schleberger, M.; Maultzsch, J. Photoluminescence of Freestanding Single- and Few-Layer MoS_2. *Phys. Rev. B* **2014**, *89* (12), 125406. https://doi.org/10.1103/PhysRevB.89.125406.

(99) Park, S.; Mutz, N.; Schultz, T.; Blumstengel, S.; Han, A.; Aljarb, A.; Li, L.-J.; List-Kratochvil, E. J. W.; Amsalem, P.; Koch, N. Direct Determination of Monolayer MoS_2 and WSe_2 Exciton Binding Energies on Insulating and Metallic Substrates. *2D Mater.* **2018**, *5* (2), 025003. https://doi.org/10.1088/2053-1583/aaa4ca.

(100) Weinhardt, L.; Fuchs, O.; Umbach, E.; Heske, C.; Fleszar, A.; Hanke, W.; Denlinger, J. D. Resonant Inelastic Soft X-Ray Scattering, x-Ray Absorption Spectroscopy, and Density Functional Theory Calculations of the Electronic Bulk Band Structure of CdS. *Phys. Rev. B* **2007**, *75* (16), 165207. https://doi.org/10.1103/PhysRevB.75.165207.

(101) Weinhardt, L.; Fuchs, O.; Fleszar, A.; Bär, M.; Blum, M.; Weigand, M.; Denlinger, J. D.; Yang, W.; Hanke, W.; Umbach, E.; Heske, C. Resonant Inelastic Soft X-Ray Scattering of CdS: A Two-Dimensional Electronic Structure Map Approach. *Phys. Rev. B* **2009**, *79* (16), 165305. https://doi.org/10.1103/PhysRevB.79.165305.

(102) Fuchs, O.; Zharnikov, M.; Weinhardt, L.; Blum, M.; Weigand, M.; Zubavichus, Y.; Bär, M.; Maier, F.; Denlinger, J. D.; Heske, C.; Grunze, M.; Umbach, E. Isotope and Temperature Effects in Liquid Water Probed by X-Ray Absorption and Resonant X-Ray Emission Spectroscopy. *Phys. Rev. Lett.* **2008**, *100* (2), 027801. https://doi.org/10.1103/PhysRevLett.100.027801.

(103) Weinhardt, L.; Fuchs, O.; Batchelor, D.; Bär, M.; Blum, M.; Denlinger, J. D.; Yang, W.; Schöll, A.; Reinert, F.; Umbach, E.; Heske, C. Electron-Hole Correlation Effects in Core-Level Spectroscopy Probed by the Resonant Inelastic Soft x-Ray Scattering Map of C60. *J. Chem. Phys.* **2011**, *135* (10), 104705. https://doi.org/10.1063/1.3633953.

(104) Eich, D.; Fuchs, O.; Groh, U.; Weinhardt, L.; Fink, R.; Umbach, E.; Heske, C.; Fleszar, A.; Hanke, W.; Gross, E. K. U.; Bostedt, C.; v. Buuren, T.; Franco, N.; Terminello, L. J.; Keim, M.; Reuscher, G.; Lugauer, H.; Waag, A. Resonant Inelastic Soft X-Ray Scattering of Be Chalcogenides. *Phys. Rev. B* **2006**, *73* (11), 115212. https://doi.org/10.1103/PhysRevB.73.115212.

(105) Fuchs, O.; Weinhardt, L.; Blum, M.; Weigand, M.; Umbach, E.; Bär, M.; Heske, C.; Denlinger, J.; Chuang, Y.-D.; McKinney, W.; Hussain, Z.; Gullikson, E.; Jones, M.; Batson, P.; Nelles, B.; Follath, R. High-Resolution, High-Transmission Soft x-Ray Spectrometer for the Study of Biological Samples. *Review of Scientific Instruments* **2009**, *80* (6), 063103. https://doi.org/10.1063/1.3133704.

(106) Carlisle, J. A.; Shirley, E. L.; Hudson, E. A.; Terminello, L. J.; Callcott, T. A.; Jia, J. J.; Ederer, D. L.; Perera, R. C. C.; Himpsel, F. J. Probing the Graphite Band Structure with Resonant Soft-X-Ray Fluorescence. *Phys. Rev. Lett.* **1995**, *74* (7), 1234–1237. https://doi.org/10.1103/PhysRevLett.74.1234.

(107) Heske, C.; Eich, D.; Fink, R.; Umbach, E.; van Buuren, T.; Bostedt, C.; Terminello, L. J.; Kakar, S.; Grush, M. M.; Callcott, T. A.; Himpsel, F. J.; Ederer, D. L.; Perera, R. C. C.; Riedl, W.; Karg, F. Observation of Intermixing at the Buried CdS/Cu(In,Ga)Se_2 Thin Film Solar Cell Heterojunction. *Appl. Phys. Lett.* **1999**, *74* (10), 1451–1453. https://doi.org/10.1063/1.123578.

(108) Lebègue, S.; Eriksson, O. Electronic Structure of Two-Dimensional Crystals from *Ab Initio* Theory. *Phys. Rev. B* **2009**, *79* (11), 115409. https://doi.org/10.1103/PhysRevB.79.115409.

(109) Kumar, A.; Ahluwalia, P. K. A First Principle Comparative Study of Electronic and Optical Properties of 1H–MoS_2 and 2H–MoS_2. *Materials Chemistry and Physics* **2012**, *135* (2–3), 755–761. https://doi.org/10.1016/j.matchemphys.2012.05.055.

(110) Wei, L.; Jun-fang, C.; Qinyu, H.; Teng, W. Electronic and Elastic Properties of MoS_2. *Physica B: Condensed Matter* **2010**, *405* (10), 2498–2502. https://doi.org/10.1016/j.physb.2010.03.022.

(111) Li, T.; Galli, G. Electronic Properties of MoS_2 Nanoparticles. *J. Phys. Chem. C* **2007**, *111* (44), 16192–16196. https://doi.org/10.1021/jp075424v.

(112) Kuc, A.; Zibouche, N.; Heine, T. Influence of Quantum Confinement on the Electronic Structure of the Transition Metal Sulfide TS_2. *Phys. Rev. B* **2011**, *83* (24), 245213. https://doi.org/10.1103/PhysRevB.83.245213.

(113) Cheng, Y.; Zhu, Z.; Schwingenschlögl, U. Role of Interlayer Coupling in Ultra Thin MoS_2. *RSC Adv.* **2012**, *2* (20), 7798. https://doi.org/10.1039/c2ra20132a.

(114) Scalise, E.; Houssa, M.; Pourtois, G.; Afanas'ev, V.; Stesmans, A. Strain-Induced Semiconductor to Metal Transition in the Two-Dimensional Honeycomb Structure of MoS_2. *Nano Res.* **2012**, *5* (1), 43–48. https://doi.org/10.1007/s12274-011-0183-0.

(115) Ramakrishna Matte, H. S. S.; Gomathi, A.; Manna, A. K.; Late, D. J.; Datta, R.; Pati, S. K.; Rao, C. N. R. MoS_2 and WS_2 Analogues of Graphene. *Angewandte Chemie International Edition* **2010**, *49* (24), 4059–4062. https://doi.org/10.1002/anie.201000009.

(116) Kadantsev, E. S.; Hawrylak, P. Electronic Structure of a Single MoS_2 Monolayer. *Solid State Communications* **2012**, *152* (10), 909–913. https://doi.org/10.1016/j.ssc.2012.02.005.

(117) Hosseini, M.; Karami, H.; Sohrabi, Z. Investigation of Layer Number Effects on the Electrical Properties of Strained Multi-Layer MoS_2. *J Comput Electron* **2019**, *18* (4), 1236–1242. https://doi.org/10.1007/s10825-019-01401-8.

(118) Kobayashi, K.; Yamauchi, J. Electronic Structure and Scanning-Tunneling-Microscopy Image of Molybdenum Dichalcogenide Surfaces. *Phys. Rev. B* **1995**, *51* (23), 17085–17095. https://doi.org/10.1103/PhysRevB.51.17085.

(119) Ellis, J. K.; Lucero, M. J.; Scuseria, G. E. The Indirect to Direct Band Gap Transition in Multilayered MoS_2 as Predicted by Screened Hybrid Density Functional Theory. *Applied Physics Letters* **2011**, *99* (26), 261908. https://doi.org/10.1063/1.3672219.

(120) Mattheiss, L. F. Energy Bands for $2H-NbSe_2$ and $2H-MoS_2$. *Phys. Rev. Lett.* **1973**, *30* (17), 784–787. https://doi.org/10.1103/PhysRevLett.30.784.

(121) Kasowski, R. V. Band Structure of MoS_2 and NbS_2. *Phys. Rev. Lett.* **1973**, *30* (23), 1175–1178. https://doi.org/10.1103/PhysRevLett.30.1175.

(122) Huisman, R.; de Jonge, R.; Haas, C.; Jellinek, F. Trigonal-Prismatic Coordination in Solid Compounds of Transition Metals. *Journal of Solid State Chemistry* **1971**, *3* (1), 56–66. https://doi.org/10.1016/0022-4596(71)90007-7.

(123) Komesu, T.; Le, D.; Zhang, X.; Ma, Q.; Schwier, E. F.; Kojima, Y.; Zheng, M.; Iwasawa, H.; Shimada, K.; Taniguchi, M.; Bartels, L.; Rahman, T. S.; Dowben, P. A. Occupied and Unoccupied Electronic Structure of Na Doped MoS_2 (0001). *Appl. Phys. Lett.* **2014**, *105* (24), 241602. https://doi.org/10.1063/1.4903824.

(124) Lee, C.; Yan, H.; Brus, L. E.; Heinz, T. F.; Hone, J.; Ryu, S. Anomalous Lattice Vibrations of Single- and Few-Layer MoS_2. *ACS Nano* **2010**, *4* (5), 2695–2700. https://doi.org/10.1021/nn1003937.

(125) Tongay, S.; Suh, J.; Ataca, C.; Fan, W.; Luce, A.; Kang, J. S.; Liu, J.; Ko, C.; Raghunathanan, R.; Zhou, J.; Ogletree, F.; Li, J.; Grossman, J. C.; Wu, J. Defects Activated Photoluminescence in Two-Dimensional Semiconductors: Interplay between Bound, Charged and Free Excitons. *Sci Rep* **2013**, *3* (1), 2657. https://doi.org/10.1038/srep02657.

(126) Seah, M. P.; Smith, G. C. Quantitative AES and XPS: Determination of the Electron Spectrometer Transmission Function and the Detector Sensitivity Energy Dependencies for the Production of True Electron Emission Spectra in AES and XPS. *Surface and Interface Analysis* **1990**, *15* (12), 751–766. https://doi.org/10.1002/sia.740151208.

(127) Weinhardt, L. Elektronische und chemische Eigenschaften von Grenzflächen und Oberflächen in optimierten $Cu(In,Ga)(S,Se)_2$ Dünnschichtsolarzellen, Universität Würzburg, 2005.

CURRICULUM VITAE

Mary Blankenship

blankenship.mh1@gmail.com

EDUCATION

Bachelor of Science in Chemistry, University of Nevada, Las Vegas (UNLV), 2021

Bachelor of Arts in Economics, University of Nevada, Las Vegas (UNLV), 2021

Minor: Brookings Public Policy

PUBLICATIONS

Journal Articles:

- Hauschild, D., Blankenship, M., Hua, A., Steininger, R., Dalibor, T. P., Eraerds, Niesen, T., Palm, J., Yang, W., Heske, C., and Weinhardt, L. "Chemical and Electronic Structure at the Interface Between a Sputter-deposited Zn(O,S) Buffer and a Cu(In,Ga)(S,Se)$_2$ Solar Cell Absorber", SolarRRL 7, 2201091 (2023). (DOI: 10.1002/solr.202201091)
- Blankenship, M., Hauschild, D., Both, L., Pyatenko, E., Witte, W., Hariskos, D., Paetel, S., Powalla, M., Weinhardt, L., Heske, C. "Conduction Band Cliff at the CdS/CuIn$_{0.1}$Ga$_{0.9}$Se$_2$ Thin-Film Solar Cell Interface." Submitted to ACS Applied Materials & Interfaces.

Articles:

- Blankenship, M., & Ordu, A U. (17 October 2022). "Russian disinformation in Africa: What's sticking and what's not." Brookings Institution. https://www.brookings.edu/blog/africa-in-focus/2022/10/17/russian-disinformation-in-africa-whats-sticking-and-whats-not/
- Blankenship, M., & Echikson, B. (17 October 2022). Conspiracy Theorists, Right-wing Politicians Fuel Nord Stream Disinformation." Center for European Policy Analysis. https://cepa.org/article/conspiracy-theorists-right-wing-politicians-fuel-nord-stream-disinformation/
- Blankenship, M., & Ordu, A U. (27 June 2022). "Russia's narratives about its invasion of Ukraine are lingering in Africa." Brookings Institution. https://www.brookings.edu/blog/africa-in-focus/2022/06/27/russias-narratives-about-its-invasion-of-ukraine-are-lingering-in-africa/
- Blankenship, M., & Graham, C. (15 June 2022). "How cynicism and misinformation add to the emotional costs of gun violence." Brookings Institution. https://www.brookings.edu/blog/up-front/2022/06/15/how-cynicism-and-misinformation-add-to-the-emotional-costs-of-gun-violence/

- Blankenship, M., & White, T. (28 August 2021). “Africa in the news: South African economy, energy production, and Nigerian foreign relations updates.” Brookings Institution. https://www.brookings.edu/blog/africa-in-focus/2021/08/28/africa-in-the-news-south-african-economy-energy-production-and-nigerian-foreign-relations-updates/
- Blankenship, M., & Golubski, C. (27 August 2021). “Figure of the week: A case study comparison of industries without smokestacks in South Africa and Uganda.” Brookings Institution. https://www.brookings.edu/blog/africa-in-focus/2021/08/27/figure-of-the-week-a-case-study-comparison-of-industries-without-smokestacks-in-south-africa-and-uganda/
- Heitzig, C., White, T., Blankenship, M. (21 August 2021). “Africa in the news: Zambian election, impacts of the Taliban’s Afghanistan takeover, and health updates.” Brookings Institution. https://www.brookings.edu/blog/africa-in-focus/2021/08/21/africa-in-the-news-zambian-election-impacts-of-the-talibans-afghanistan-takeover-and-health-updates/
- Blankenship, M., & Golubski, C. (20 August 2021). “Figure of the week: Potential for youth and female employment in industries without smokestacks.” Brookings Institution. https://www.brookings.edu/blog/africa-in-focus/2021/08/20/figure-of-the-week-potential-for-youth-and-female-employment-in-industries-without-smokestacks/
- White, T., & Blankenship, M. (14 August 2021). “Africa in the news: Ethiopia updates, Zambia elections, and Africa’s many Olympic achievements.” Brookings Institution. https://www.brookings.edu/blog/africa-in-focus/2021/08/14/africa-in-the-news-ethiopia-updates-zambia-elections-and-africas-many-olympic-achievements/
- Blankenship, M., & Golubski, C. (11 August 2021). “Nigeria’s Twitter ban is a misplaced priority.” Brookings Institution. https://www.brookings.edu/blog/africa-in-focus/2021/08/11/nigerias-twitter-ban-is-a-misplaced-priority/
- Heitzig, C., Blankenship, M., & White, T. (07 August 2021). “Africa in the news: Politics, security, and wildlife poaching updates.” Brookings Institution. https://www.brookings.edu/blog/africa-in-focus/2021/08/07/africa-in-the-news-politics-security-and-wildlife-poaching-updates/
- Blankenship, M., Holtz, L., & White, T. (17 July 2021). “Africa in the news: Natural resource update, security updates, and COVID-19’s third wave in Africa.” Brookings Institution. https://www.brookings.edu/blog/africa-in-focus/2021/07/17/africa-in-the-news-natural-resource-update-security-updates-and-covid-19s-third-wave-in-africa/
- Blankenship, M., Holtz, L., & White, T. (10 July 2021). “Africa in the news: COVID-19 spreads, Jacob Zuma sentenced, and climate change mitigation efforts enhanced.” Brookings Institution. https://www.brookings.edu/blog/africa-in-focus/2021/07/10/africa-in-the-news-covid-19-spreads-jacob-zuma-sentenced-and-climate-change-mitigation-efforts-enhanced/

- White, T., Holtz, L., Blankenship, M. (03 June 2021). “Africa in the news: Eswatini protests, upgrades to Rwanda’s health system, and energy and environment updates.” Brookings Institution. https://www.brookings.edu/blog/africa-in-focus/2021/07/03/africa-in-the-news-eswatini-protests-upgrades-to-rwandas-health-system-and-energy-and-environment-updates/
- Holtz, L., Blankenship, M., & White, T. (26 June 2021). “Africa in the news: A COVID-19 third wave, solar energy in Togo, and security updates.” Brookings Institution. https://www.brookings.edu/blog/africa-in-focus/2021/06/26/africa-in-the-news-a-covid-19-third-wave-solar-energy-in-togo-and-security-updates/
- White, T., Holtz, L., Blankenship, M. (19 June 2021). “Africa in the news: COVID-19, Côte d’Ivoire, and energy updates.” Brookings Institution. https://www.brookings.edu/blog/africa-in-focus/2021/06/19/africa-in-the-news-covid-19-cote-divoire-and-energy-updates/
- Blankenship, M., & Golubski, C. (18 June 2021). “Figure of the week: Increasing access to electricity in sub-Saharan Africa.” Brookings Institution. https://www.brookings.edu/blog/africa-in-focus/2021/06/18/figure-of-the-week-increasing-access-to-electricity-in-sub-saharan-africa/
- Holtz, L., White, T., Blankenship, M. (12 June 2021). “Africa in the news: Elephant overpopulation in Zimbabwe, famine in Tigray, and Twitter ban in Nigeria.” Brookings Institution. https://www.brookings.edu/blog/africa-in-focus/2021/06/12/africa-in-the-news-elephant-overpopulation-in-zimbabwe-famine-in-tigray-and-twitter-ban-in-nigeria/
- Blankenship, M., & Graham, C. (5 May 2021). “Assessing the social and emotional costs of mass shootings with Twitter data.” Brookings Institution. https://www.brookings.edu/blog/up-front/2021/05/05/assessing-the-social-and-emotional-costs-of-mass-shootings-with-twitter-data/
- Blankenship, M., & Reeves, R. (10 July 2020). “From the George Floyd moment to a Black Lives Matter movement, in tweets.” Brookings Institution. https://www.brookings.edu/blog/up-front/2020/07/10/from-the-george-floyd-moment-to-a-black-lives-matter-movement-in-tweets/
- Blankenship, M., & Graham, C. (6 July 2020). “How misinformation spreads on Twitter.” Brookings Institution. https://www.brookings.edu/blog/up-front/2020/07/06/how-misinformation-spreads-on-twitter/
- “Guest column: More can be done to incentivize renewable energy.” (26 October 2019). Las Vegas Sun. https://lasvegassun.com/news/2019/oct/26/more-can-be-done-to-incentivize-renewable-energy/
- Hansen, M., Breazeale, G., Blankenship, M. (17 July 2019). “STEM teachers are most in need of additional pay.” Brookings Institution. https://www.brookings.edu/blog/brown-center-chalkboard/2019/06/17/stem-teachers-are-most-in-need-of-additional-pay/

Opinion Pieces:

- “Where I Stand: Information pollution is choking our humanity.” (13 September 2023). Las Vegas Sun. https://lasvegassun.com/news/2023/sep/11/information-pollution-is-choking-our-humanity/
- “In an age of misinformation, fact-checking must be encouraged.” (13 June 2020). Las Vegas Sun. https://lasvegassun.com/news/2020/jun/13/in-an-age-of-misinformation-fact-checking-must-be/
- “Lincoln Memorial reminds us who we are and can still be.” (3 November 2018). Las Vegas Sun. https://lasvegassun.com/news/2018/nov/03/lincoln-memorial-reminds-us-who-we-are-and-can-sti/
- “Embrace the connectivity of the global machine.” (30 June 2018). Las Vegas Sun. https://lasvegassun.com/news/2018/jun/30/embrace-the-connectivity-of-the-global-machine/

Fact Sheets:

- Vong, A., Billot, Z., Blankenship, M., Saladino, C. J., Brown, W. E. (2023). Twitter Trends During the 82nd Session of the Nevada Legislature, 2023. Elections & Governance Fact Sheet No. 7 1-4. https://digitalscholarship.unlv.edu/bmw_lincy_elect/7
- Blankenship, M., Saladino, C.J., Brown, W.E. (2022). Ukraine-Russia War: Nevada Twitter and Disinformation Trends. Elections & Governance Fact Sheet No. 3, 1-4. https://digitalscholarship.unlv.edu/bmw_lincy_elect/3
- Leclair, A., Blankenship, M., Saladino, C., Brown, W. E. (2020). Migration of Millennials and Seniors in the Mountain West. Demography Fact Sheet No. 5 1-3. https://digitalscholarship.unlv.edu/bmw_lincy_demography/5
- Blankenship, M., Saladino, C., Brown, W. E. (2020). COVID-19: Economic Recovery, Twitter, and Public Perception of Las Vegas. Economic Development & Workforce Fact Sheet No. 18 1-6. https://digitalscholarship.unlv.edu/bmw_lincy_econdev/18
- Blankenship, M., Saladino, C., Brown, W. E. (2020). How Startups Help Cities Measure Their Economic Development Frontier. Economic Development & Workforce Fact Sheet No. 16 1-2. https://digitalscholarship.unlv.edu/bmw_lincy_econdev/17
- Blankenship, M., Saladino, C., Brown, W. E. (2020). Signs of Digital Distress: The Mountain West. Transportation & Infrastructure Fact Sheet No. 3 1-3. https://digitalscholarship.unlv.edu/bmw_lincy_trans/2
- Smith, E., Blankenship, M., Saladino, C., Brown, W. E. (2020). Foot Traffic & Walkable Urbanism. Transportation & Infrastructure Fact Sheet No. 2 1-5. https://digitalscholarship.unlv.edu/bmw_lincy_trans/1
- Blankenship, M., Saladino, C., Brown, W. E. (2020). How Technology-Based Start-Ups Support U.S. Economic Growth. Economic Development & Workforce

Fact Sheet No. 12 1-13.
https://digitalscholarship.unlv.edu/bmw_lincy_econdev/13

- Blankenship, M., Saladino, C., Brown, W. E. (2019). Digitalization and the American Workforce. Economic Development & Workforce Fact Sheet No. 7 1-5. https://digitalscholarship.unlv.edu/bmw_lincy_econdev/7

Capstone:

- Blankenship, M. (2020). How Misinformation Spreads Through Twitter. 1-28. https://digitalscholarship.unlv.edu/brookings_capstone_studentpapers/6

PRESENTATIONS:

Keynote Address:

- Fall 2020 Research Symposium. University of Nevada, Las Vegas. http://oursymposium.sites.unlv.edu/keynote-speaker-mary-blankenship/

Talk requested by organizers:

- Blankenship, M., van Maris, V., Hauschild, D., Witte, W., Hariskos, D., Yang, W., Blum, M., Powalla, M., Weinhardt, L., & Heske, C. (2020, May). *Chemical and electronic properties of buffer/Cu(In,Ga)*Se_2 *interfaces with varying Ga/(Ga+In) absorber ratios.* Virtual Chalcogenide PV Conference 2020. Online.

Talks:

- Blankenship, M., Jacobellis, B., Hauschild, D., Weinhardt, L., Khan, I., Muzzillo, C., Zakutayev, A., Gaillard, N., & Heske, C. (2023, April). *Chemical and electronic properties of* $Mg_xZn_{1-x}O/CuGa_3Se_5$ *interface with a* Cd^{2+}*-Treatment.* Materials Research Society 2023 Spring Meeting. San Francisco, California
- Blankenship, M., Hauschild, D., Pyatenko, E., Witte, W., Hariskos, D., Paetel, S., Powalla, M., Weinhardt, L., & Heske, C. (2021, May). *Impact of RbF-Post-Deposition Treatments on the Chemical and Electronic Structure of Cu(In,Ga)*Se_2 *Surfaces and CdS/Cu(In,Ga)*Se_2 *Interfaces with high Ga/(Ga+In) Ratio.* European Materials Research Society 2021 Spring Meeting. Online.
- Blankenship, M., Hauschild, D., Pyatenko, E., Witte, W., Harikos, D., Yang, W., Blum, M., Powalla, M., Weinhardt, L., & Heske, C. (2021, April). *Chemical and electronic properties of CdS/Cu(In,Ga)*Se_2 *interfaces with high Ga/(Ga+In) ratio and post-deposition treatment.* Materials Research Society 2021 Spring Meeting. Online.
- Blankenship, M., Hauschild, D., Carter, J., van Maris, V., Witte, W., Hariskos, D., Yang, W., Blum, M., Powalla, M., Weinhardt, L., & Heske, C. (2018, June). *Chemical and electronic properties of the CdS/Cu(In,Ga)*Se_2 *interface with varying Ga/(Ga+In) absorber ratios.* European Materials Research Society 2018 Spring Meeting. Strasbourg, France.

- Blankenship, M. (2019, April*). Surface and interface properties of $CdS/Cu(In,Ga)Se_2$ thin-film solar cells with varying Ga/(Ga+In) absorber ratios.* Spring Undergraduate Research Conference. Las Vegas, Nevada.
- Blankenship, M., the Heske Team. (2017, November). *Chemical surface structure of $Cu(In,Ga)Se_2$ absorbers for thin-film solar cells*. Undergraduate Research Slam. Las Vegas, Nevada.
- Blankenship, M., the Heske Team. (2017, August). *Chemical surface structure of $Cu(In,Ga)Se_2$ absorbers for thin-film solar cells*. Undergraduate Research Symposium. Las Vegas, Nevada.

- Blankenship, M., (2020, November). *How Misinformation Spreads on Twitter: A Case Study on the 1 October Mass Shooting.* Undergraduate Research Symposium. Las Vegas, Nevada.
- Blankenship, M., (2019, October). *Using Tweets to Analyze the Social Costs of Mass Shootings.* Honors+Research Symposium. Las Vegas, Nevada.
- Graham, C., & Blankenship, M. (2018, November). *The Unobservable Costs of Gun Violence in America: Lessons from the New Science of Well-Being.* Reflecting on 1 October: Research to Heal Our Community Symposium. UNLV Public Lecture. Las Vegas, Nevada.

Posters:

- Blankenship, M., Jacobellis, B., Hua, A., Hauschild, D., Weinhardt, L., Khan, I., Muzzillo, C., Zakutayev, A., Gaillard, N., & Heske, C. (2023, April). *Chemical and electronic structure of Cd^{2+}-treated $CuGa_3Se_5$ solar absorbers and their interfaces with $Mg_xZn_{1-x}O$ buffers.* Graduate and Professional Student Association Research Forum. Las Vegas, Nevada.
- Blankenship, M., Jacobellis, B., Hua, A., Hauschild, D., Weinhardt, L., Khan, I., Muzzillo, C., Zakutayev, A., Gaillard, N., & Heske, C. (2022, May). *Chemical and electronic structure of Cd^{2+}-treated $CuGa_3Se_5$ solar absorbers and their interfaces with $Mg_xZn_{1-x}O$ buffers.* Materials Research Society 2022 Spring Meeting. Honolulu, Hawai'i.
- Blankenship, M., Carter, J., Hauschild, D., Witte, W., Hariskos, D. Powalla, M., Blum, M., Weinhardt, L., Heske, C. (2017, November). *Chemical surface structure of $Cu(In,Ga)Se_2$ absorbers for thin-film solar cells*. American Chemical Society Southern Nevada annual poster competition. Las Vegas, Nevada.
- Blankenship, M., Graham, C. (2021, January). *How Misinformation Spreads on Twitter: A Case Study on the 1 October Mass Shooting.* National Collegiate Research Conference, Harvard College. Online.

HONORS & AWARDS:

2023
- UNLV's Presidential Innovation Challenge finalist, Team Scarlet and Green, $1100
- UNLV's Presidential Innovation Challenge competition, 3rd place, $10000
- UNLV's Presidential Innovation Challenge competition scholarship, $750
- GPSA 2023 Research Forum, 2nd place in poster competition, $250

2022
- GPSA Sponsorship Research & Travel Grant, $1250
- Best Poster Award in Symposium EN03: Emerging Inorganic Semiconductors for Solar Energy and Fuels at MRS 2022, $400

2021
- UNLV Winter 2021 Commencement Student Speaker, https://www.youtube.com/watch?v=oF3RhKjo8y4
- Honors College Medallion Ceremony Student Speaker
- Outstanding Student Service Award – Honors College
- Oral Presentation winner in Symposium EN07: Advances in CIGS/CZTS Solar Cells at MRS 2021 3rd place, $200

2020
- 2020 Outstanding Undergraduate Researcher, Office of Undergraduate Research, $500 http://oursymposium.sites.unlv.edu/outstanding-undergraduate-researcher-award/
- Summer Undergraduate Research Funding Scholarship, $1000 (for Chemistry research)
- Summer Undergraduate Research Funding Scholarship, $1000 (for Policy research)

2019
- 1st Place in the Science and Engineering Podium Presentations Session at the Spring Undergraduate Research Conference, $250
- Summer Undergraduate Research Funding Scholarship sponsored by the Consolidated Students of the University of Nevada, $1000
- OUR Travel Fund, $500
- Lee Business School Dean's Honor Roll

2018
- Summer Undergraduate Research Funding Scholarship sponsored by the Lee Business School, $1500
- OUR Travel Fund, $500

2017
- 1st place in American Chemical Society, Southern Nevada American Chemical Society annual poster competition, $300
- Undergraduate Research Slam, semi-finalist in a lighting talk competition
- Undergraduate Research Stipend for the 2017-2018 academic year, $5000
- Summer Undergraduate Research Funding Scholarship sponsored by the Honors College, $1500

TEACHING EXPERIENCE:

(Fall 2023)	Physical Chemistry Laboratory
(Spring 2023)	Chemistry 121L Laboratory
(Fall 2022)	Physical Chemistry Laboratory
(Spring 2022)	Chemistry 121L Laboratory

RESEARCH EXPERIENCE:

(2022 – Present) Graduate Research Assistant, Department of Chemistry and Biochemistry, University of Nevada, Las Vegas

- Principal Investigator: Dr. Clemens Heske

(2017 – 2022) Undergraduate Research Assistant, Department of Chemistry and Biochemistry, University of Nevada, Las Vegas

- Principal Investigator: Dr. Clemens Heske
  - Research utilizes a “tool chest” of spectroscopic techniques, located at UNLV and the Advanced Light Source (ALS), Lawrence Berkeley National Laboratory (LBNL)
  - The goal of the research is to analyze the chemical and electronic properties of Cu(In,Ga)Se_2 solar cells with our collaboration partner ZSW (Center for Solar Energy and Hydrogen Research Baden-Württemberg, Stuttgart, Germany)

(6/14 - 7/22 2018) Visiting Scientist, Karlsruhe Institute of Technology, Germany

(2022 – Present) Graduate Student Researcher, Brookings Mountain West

- Research policy issues related to science, technology, and social media in the Mountain West states

(9/7 - 12/6 2022) Contributor, Center for European Policy Analysis

- Digital Innovation Initiative

(2019 – 2022) Student Researcher, Brookings Mountain West

(6/7 - 8/27 2021) Intern, African Growth Initiative, Brookings Institution

- Global Economy and Development Program
- Conducted research on environmental, energy, and tech-related issues in Africa with Senior Fellow and Director Dr. Aloysius Ordu
- Collected and analyzed over 250 million tweets concerning COVID-19 from March ’20 to August ‘21 to identify online misinformation

(7/28 - 8/17 2019) Visiting Researcher, Brookings Institution

  - Continued research on mass shootings with Dr. Carol Graham
  - Set up collections of over 50 million tweets concerning mass shootings, used econometric and sentiment analysis to uncover the social costs of mass shootings in the United States

(5/15 - 6/12 2018) Intern (ad hoc), Brookings Institution

  - Global Economy and Development Program
  - Conducted research on the social costs of mass shootings in communities with Leo Pasvolsky Senior Fellow, Dr. Carol Graham

(2017 – 2019) Research Ambassador, UNLV Office of Undergraduate Research

(Fall 2018) Research Consultant, UNLV Office of Undergraduate Research